Interpolation of velocity fields with Delaunay tessellations

Liesbeth Vermaas
Supervisor: Prof. dr. M.A.M. van de Weijgaert

September 24, 2004

[1]

---

[1] het plaatje is van Escher

Contents

Introduction

The aim of this research project was to compare different interpolation methods for the results of N-body simulations. It is known that in these simulations normally the material 'clutches' together, in such a way that foam-like structures are formed with walls and voids. When trying to describe the (continuous) peculiar velocity field by interpolation of the velocities of the particles there are several problems to deal with. Especially in the empty regions (voids), normal interpolation does not work properly. When the underlying velocity field of the simulations can be described accurately and at any point, the motions will be better understood which therefore leads to a better understanding of the formation of the large scale structure: galaxies and clusters of galaxies. Using Voronoi-tessellations has proved to be valuable in the past with densities. In this research project a similar procedure, the Delaunay-tessellation, is used for estimating the velocities resulting from N-body simulations and the results are be compared to those of TSC-interpolation. First, a short overview of cosmology and observations is given in chapter 1 followed by the somewhat more thorough chapters about structure formation in the universe (chapter 2) and computational techniques in this field (chapter 3). Chapter 4 gives the details of this research project with a discussion of the results and conclusions.

Chapter 1

Cosmology and Large Scale Structure

Visible material in the universe at some scale is clearly not homogeneously distributed. Most obviously recognized are discrete objects like stars and galaxies, but there are also structures like clusters of galaxies and even larger, the superclusters. One major question in science is (and has been in the past) that of the history of the universe. Advancing technology allows us to get an increasingly detailed view, providing information for the development of theories of the origin of this universe. A widely accepted theory among most scientists is that of the *Big Bang*, which states that matter originates from energy and was blown away in all directions in a moment of 'explosion'. This chapter is divided in two sections, the first section summarizes some basic properties of Big Bang-cosmology, the second part gives an overview of observational studies in this field.

1.1 History and basics of cosmology

Scientists did not always believe that there was a Big Bang. The main historical idea was that of a static universe that had always existed, in which galaxies remain in their places. Newton already noted that all objects attract each other and without any other force would fall together. He wondered whether some large-scale motion could compensate this fact. Still, the universe was assumed to be static at the time Einstein published his theory of general relativity in 1916, and his equations were also based on this idea. He introduced his *cosmological constant* (Λ) as an arbitrary outward force to prevent the gravitational infall of matter. But Friedmann (in 1922) and Lemaître (in 1927) independently found two other solutions to the equations could that not be excluded: that of a contracting and that of an expanding universe. Although Einstein first claimed that Friedmann was wrong, calling the cosmological constant 'the greatest blunder in his life', in the next year he admitted his 'mistake' to Friedmann in a two-sentence paper [14].

Hubble's law

Only after Hubble's discovery in 1929 that (almost) all galaxies are moving away from us with velocities proportional to their distance from earth [17], the idea of an expanding universe was set. This was consistent with the Cosmological Principle formulated by Einstein before, which states that the universe is isotropic and on large enough scale homogeneous. The outward motion of a galaxy results in a Doppler-shift of the emitted light to the red part of the spectrum, this shift is the *redshift*, z. In formula form, the redshift of a galaxy is:

$$z = \frac{\lambda(t) - \lambda_0}{\lambda_0} \tag{1.1}$$

$\lambda(t)$ is the observed wavelength, λ_0 is the emitted wavelength. Now Hubble's law can be stated as

$$\mathrm{c}z = H_0 \mathrm{r} \tag{1.2}$$

where c is the (constant) speed of light, r is the distance to the object and H_0 is the Hubble constant. At this time the estimate for H_0 was 50 - 100 km $\mathrm{s}^{-1}\mathrm{Mpc}^{-1}$, recent observations can predict this value with more precision (section 1.2). However, for high velocities this is not valid and a relativistic form of the formula has to be used.

If we go back in time, all material moves closer toghether, up to a point in time when it was all concentrated in one single point. This point, or rather singularity, in space-time is what is called the Big Bang. The relative size of the universe at different times can be expressed in terms of a *scale factor*, $a(t)$. In an expanding universe, $a(t)$ is zero at the Big Bang and increases with time. The scale factor *scales* distances (or lengths) in time, such that these are constant for any set of points that flow with the Hubble expansion. This is called the *comoving distance* in *comoving space*. If $\vec{r}$ denotes the physical location in space, its comoving coordinate $\vec{x}$ is defined as $\vec{x}(t) = \frac{\vec{r}}{a(t)}$. The relation between the Hubble constant and the scale factor is thus:

$$H(t) = \frac{\dot{a}(t)}{a(t)} \tag{1.3}$$

$$H_0 = \left.\frac{\dot{a}}{a}\right|_{t=t_0} \tag{1.4}$$

where a is the scale factor, $\dot{a}$ is the time derivative of a and t_0 is the present time. The redshift and the scale factor can now be linked:

$$1 + z = \frac{\lambda_t}{\lambda_0} = \frac{a(t)}{a(t_0)} \tag{1.5}$$

Note that, similar to the Hubble law, the relation in this form is only valid for low redshifts; when the velocity becomes larger one has to take into account relativistic effects.

Friedmann-Robertson-Walker Universe

Assuming the Cosmological Principle (homogeneous and isotropic universe), the expression for a line element (ds) can be expressed in spherical coordinates (r, θ, ϕ)

$$\mathrm{d}s^2 = \mathrm{c}^2\mathrm{d}t^2 - a^2(t)\left[\frac{\mathrm{d}r^2}{1-kr^2} + r^2(\mathrm{d}\theta^2 + \sin^2\theta\mathrm{d}\phi^2)\right] \tag{1.6}$$

this is called the Friedmann-Robertson-Walker metric, after the men who first wrote it down. With this they introduce the curvature constant k (an integration constant from the Einstein equations), $k = 0$ means a flat universe: with Euclidean geometry for the three spatial dimensions. Combining this metric with General Relativity and the ideal fluid approximation gives these two equations, that mark the Friedmann-Lemaître cosmological model:

$$\frac{\ddot{a}}{a} = \frac{4}{3}\pi G\left(\rho + \frac{3p}{\mathrm{c}^2}\right) + \frac{\Lambda}{3} \tag{1.7}$$

$$H^2 = \left(\frac{\dot{a}}{a}\right)^2 = \frac{8}{3}\pi G\rho + \frac{k\mathrm{c}^2}{a^2} + \frac{\Lambda}{3} \tag{1.8}$$

H is the Hubble constant, here as a function of time, G is Newton's gravitational constant, Λ is the cosmological constant, ρ is the overall density of the universe and k is the curvature constant. The size, shape and fate of the universe highly depend on the different values for these parameters. As mentioned before, zero curvature indicates a flat universe; the expansion rate will at some point stay the same forever. An open universe means that the expansion will keep on growing: $k < 0$ and $a(t)$ stays positive. In a closed universe ($k > 0$) the expansion will decrease to zero. Here some useful quantities to work with are ρ_{cr}, the critical density of the universe, and Ω, a dimensionless cosmological density parameter. These are defined by

$$\rho_{cr} \equiv \frac{3H_0^2}{8\pi G} \tag{1.9}$$

$$\Omega = \frac{\rho}{\rho_{cr}}; \quad \Omega_0 = \frac{\rho_0}{\rho_{cr}} \tag{1.10}$$

The critical density is the density that exactly divides between the open and closed universe. The value of Ω_0 is less than unity for an open universe, greater than unity for a closed universe and exactly one for a flat universe. The total density is the sum of all various contributions to the density: $\Omega = \Sigma\ \Omega_i$. The major contributions are matter (Ω_m) and radiation (Ω_r). With a nonzero cosmological constant, and a contribution of the vacuum energy to the cosmological density of

$$\Omega_\Lambda \equiv \frac{\Lambda}{3H_0^2} \tag{1.11}$$

the universe is flat for $k = 0$, which implies that $\Omega_m + \Omega_\Lambda = 1$, while radiation is considered negligible (instead of Λ as a subscript, sometimes v is used, which stands for vacuum). Nevertheless, the existence of the cosmological constant is nontrivial and this problem has not been resolved yet (Figure 1.1)[1]. Hence, the explanation for what Λ should be is unclear: mostly it is referred to as vacuum energy or dark energy. For a review on the cosmological constant problem see Carroll, Press and Turner, 1992 [9]. A constant curvature universe obeying the cosmological principle with zero cosmological constant is called an *Einstein-de Sitter* universe (in contrast with the *Friedmann-Lemaitre* universe).

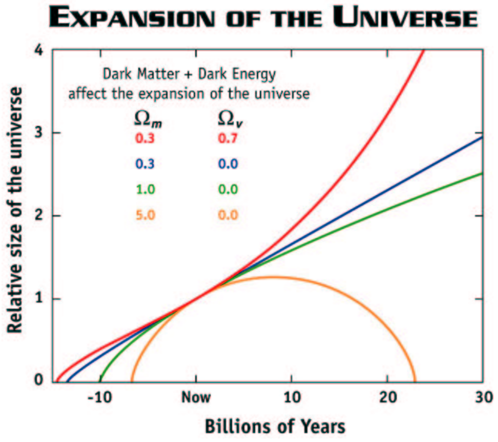

Figure 1.1: Possible scenarios for the expansion (and possibly contraction) of the universe: the bottom orange curve represents a closed, high density universe which expands for several billion years, then ultimately turns around and collapses under its own weight. The green curve represents a flat, critical density universe in which the expansion rate continually slows down (the curves becomes ever more horizontal). The blue curve shows an open, low density universe whose expansion is also slowing down, but not as much as the previous two because the pull of gravity is not as strong. The top (red) curve shows a universe in which a large fraction of the matter is in a form dubbed "dark energy" which is causing the expansion of the universe to accelerate. There is growing evidence that our universe is following the red curve. Courtesy figure and caption: WMAP website[1]

---

[1] `http://map.gsfc.nasa.gov/m_uni/uni_101fate.html`

Table 1.1: Some cosmological parameters: different values for different models in a Friedmann-Robertson-Walker-Lemaître universe.

shape	**curvature**	**volume**	**density**
closed	$k > 0$	finite	$\Omega_0 > 1$
flat	$k = 0$	infinite	$\Omega_0 = 1$
open	$k < 0$	infinite	$\Omega_0 < 1$

There are more unresolved problems stemming from this standard Big Bang theory, of which the most remarkable are the *flatness problem* and the *horizon problem*. The first refers to the fact that the measurements for Ω_0 give a value very close to unity, while this is an unstable solution: for this value the initial conditions of the universe must have been very fine-tuned. The horizon problem concerns the observed large scale isotropy of the cosmic microwave background radiation, which cannot be explained in combination with the size of causally connected regions at the moment of recombination which subtends only a few degrees on the sky [32]. The estimated values of some important cosmological parameters in different models are put together in Table 1.1.

Models for the early Universe

Theories trying to solve these issues involve the inflation-model which states that in the very early universe there was a period in which a super-cooled phase transition caused the vacuum energy density to become dominant. If this period is long enough, the curvature term can become small and the result is a globally flat universe. Also, as the universe could 'inflate' from a region that was causally connected and in thermal contact, the horizon problem is solved this way [32]. The consequence of an inflationary universe, however, is that it requires a much larger value of Ω_0 than is observed in observable matter. Thus, there is a need for a 'missing matter' component that we cannot see: dark matter. There are more indications, from recent observations of motions of galaxies and galactic dynamics, that this component exists, but there is no certainty about the material that would make up this dark matter. The total matter density is then

$$\Omega_{m,0} = \Omega_{B,0} + \Omega_{M,0} \tag{1.12}$$

with Ω_B for baryonic 'normal' matter and Ω_M for non-baryonic dark matter. About 80% of all matter could be non-baryonic. Two options for the nature of dark matter are Hot Dark Matter (HDM) and Cold Dark Matter (CDM). HDM consists of collisionless particles with a large velocity dispersion, CDM consists of collisionless particles with very small velocity dispersion. The nature of the dark matter highly influences the way of structure formation. Presently, observations seem to favour a cosmological model with Cold Dark Matter and a nonzero cosmological constant (ΛCDM) with $\Omega_\Lambda = 0.7$ and $\Omega_m = 0.3$.

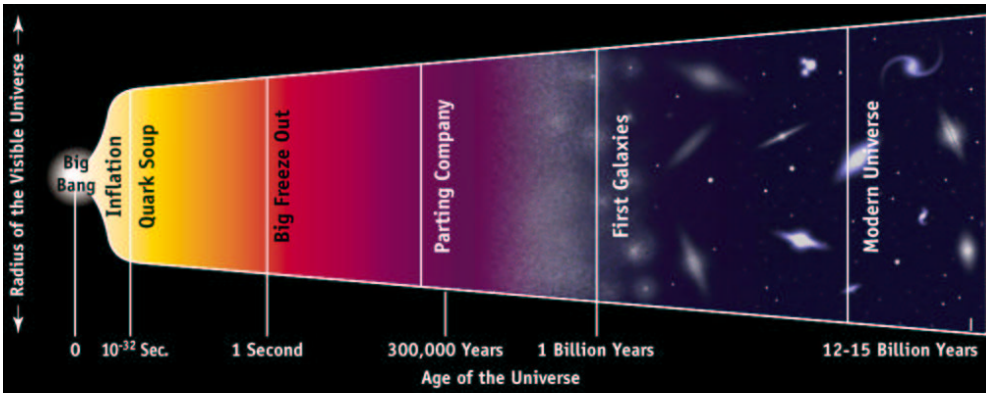

Figure 1.2: Space, time and structure from the Big Bang until now.

The commonly accepted model is the 'hot Big Bang model', in which after the Big Bang the universe consisted of hot, uniformly distributed gas/plasma at first, a *radiation dominated* universe mainly consisting of protons, electrons and photons. This universe cooled due to expansion, making it possible for elements, and later molecules to form, eventually becoming the *matter dominated* universe we presently live in. The separation between radiation-domination and matter-domination is called the epoch of equivalence. This is possible because matter and radiation evolve in different ways, and the moment for their densities being equal is at about $z = 1000$. Very short after this moment of matter taking over the universe, radiation and matter decoupled. This marks the epoch of recombination: nuclei and electrons formed atoms, no longer scattering the photons. It is only from this moment of transparancy that photons could freely escape, and therefore it is not possible for us to look back further in time: the electron density is too high at higher redshifts for the photons to escape scattering.

1.2 Observations of large scale structure

Observational studies show in detail what the universe looks like in our neighbourhood. But the further we look, the further back in time it is since the light of very distant galaxies reaches us only with the finite speed of light. This way we can actually look back in time and try to find out what really happened.

1.2.1 Galaxy distribution

By just observing the sky as deep as possible, counting and mapping the galaxies in all directions on the sky gives a two-dimensional impression of the galaxy distribution. The first survey was APM (Maddox et al. 1990, 1996 [19, 20])[2] followed-up by the infrared survey of 2MASS (Figure 1.3)[3].

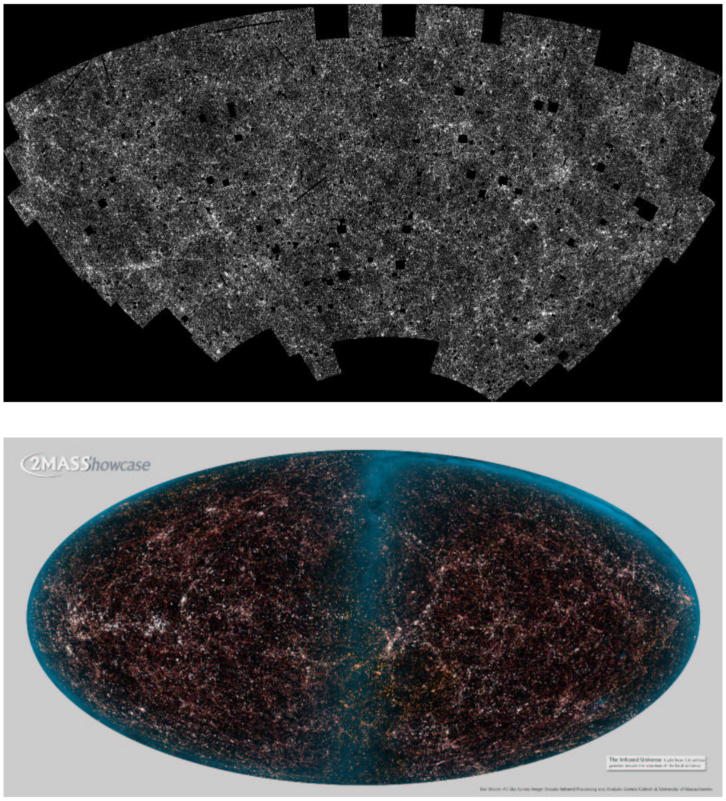

Figure 1.3: The galaxy distribution on the sky. Top: part of the sky by the APM galaxy survey[2]. Courtesy: Steve Maddox, Will Sutherland, George Efstathiou and Jon Loveday. Bottom: whole sky distribution by the infrared 2MASS survey[3]. Visible are many galactic clusters and superclusters, as well as some streamers composing the large-scale structure of the nearby universe. The blue overlay represents the very close and bright stars from our own Milky Way galaxy.

---

[2] `http://www.nottingham.ac.uk/~ppzsjm/apm/apm.html`

[3] `http://pegasus.phast.umass.edu/frame.html`

A number of deep surveys was dedicated to measuring the galaxies' redshifts in order to extend the maps into the third dimension. One-dimensional redshift surveys are the 'pencil beam' surveys, which go deep on a very small region of sky. Two- and three-dimensional surveys give slices of the universe, with increasing thickness. The first influential of these, the CfA2 slice, gave an impression of the local three-dimensional universe (De Lapparent et al. 1986 [11])[4]. Several studies followed using the continuously advancing equipment and more powerful telescopes. These include the Las Campanas Redshift Survey (Shectman et al. 1996 [31])[5], and the 2dF Galaxy Redshift Survey (Colles et al. 1999 [10])[6]. Figure 1.4 shows a comparison of the CfA and the 2dF results.

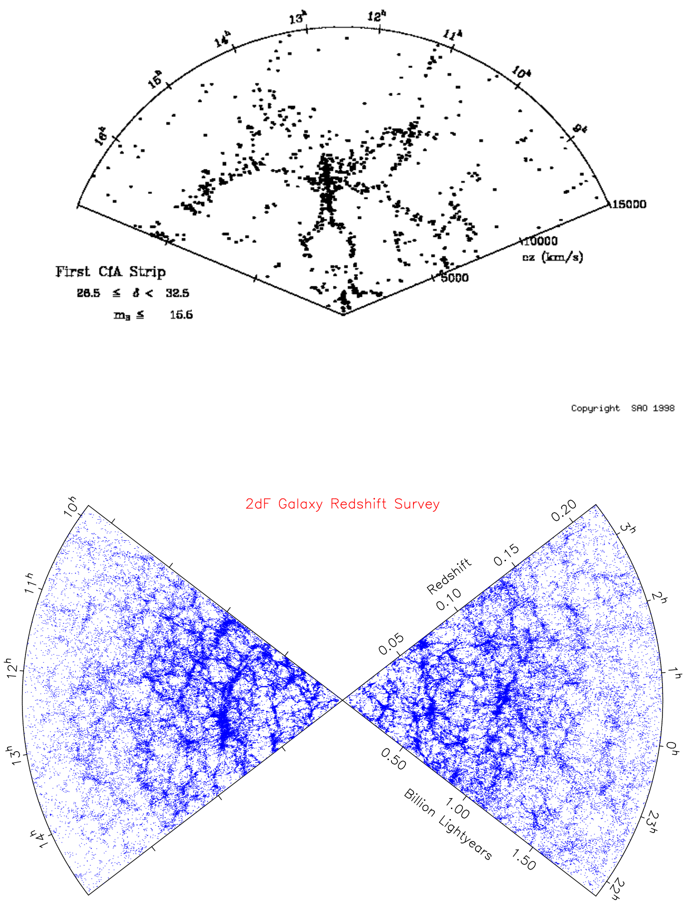

Copyright SAO 1998

Figure 1.4: Galaxy redshift surveys: slice of the CfA galaxy redshift survey[4] (top) and of the 2dF galaxy redshift survey[6] (bottom). Note the difference in scale: CfA is limited by $z \sim 0.05$, while 2dF goes out to $z \sim 0.25$!

---

[4] `http://cfa-www.harvard.edu/~huchra/zcat/`

[5] `http://qold.astro.utoronto.ca/~lin/lcrs.html`

[6] `http://www.mso.anu.edu.au/2dFGRS/`

Table 1.2: Details of the different Galaxy Redshift Surveys.

Redshift Survey	**# galaxies**	**redshift**
CfA	~ 2400	0.05
Las Campanas	~ 26000	0.1
2dF	~ 140000	0.25
SDSS	$\sim$ 1 million	0.2/0.5

The most recent study is the Sloan Digital Sky Survey (SDSS)[7], of which Figure 1.5 shows the first results. Table 1.2 gives more details of these redshift surveys.

In all of these studies it is clearly seen that the galaxies are not distributed in a homogeneous way at all, but are rather in clusters and filaments with (nearly) spherical empty spaces in between (*voids*), it is a *foam-like* structure. The filaments of these large-scale inhomogeneities can have sizes of 100 - 200 h^{-1}Mpc, while the voids measure about 20 - 50 h^{-1}Mpc.

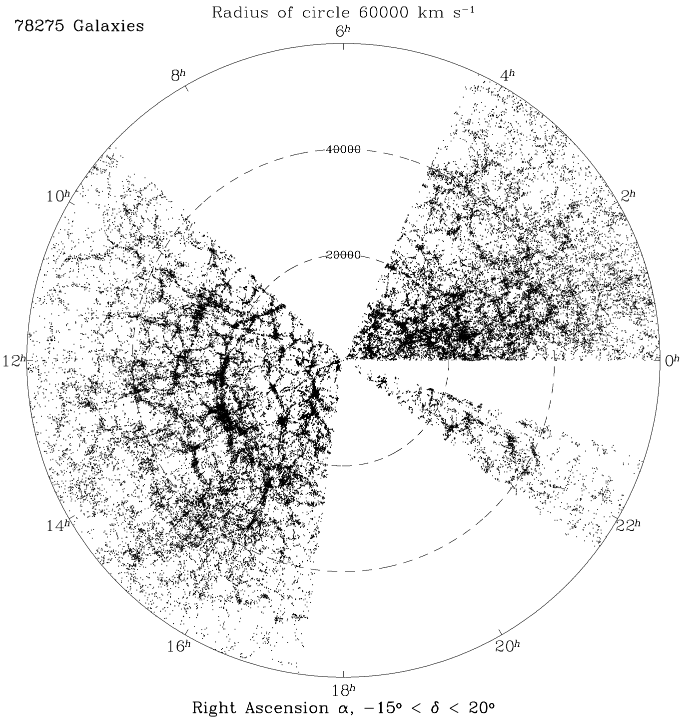

Figure 1.5: The distribution of 10,853 galaxies in a small slice of the SDSS main survey[7], along with another 486 "luminous red galaxies", chosen to map out structure to higher redshifts (only 1% of the expected final spectroscopic data). The bubble-like network of walls, filaments, and voids is clearly visible. Courtesy: A. Pope, JHU.

---

[7] `http://www.sdss.org/`

1.2.2 Cosmic Background Radiation

Although we see the galaxies being very far away, this is still local universe compared to the distant Big Bang. To get a clue about the Big Bang theory, more distant information is needed. Assuming the hot Big Bang theory (mentioned in section 1.1), Gamow, Alpher and Hermann (1940) calculated the relative abundances of hydrogen and helium that would be produced in this scenario. This happened to be consistent with the observations, later on also the abundances of other light elements were found to be consistent. Moreover, Alpher and Hermann had predicted the presence of afterglow-radiation originating from the Big Bang itself, and this indeed was (accidentally) observed by the physicists Penzias and Wilson in 1965 [24], while the scientific explanation was given in a separate paper by Dicke, Peebles, Roll and Wilkinson [13]. This 'echo'-radiation, unlike the structure in the galaxy-redshift surveys, is homogeneous and generally flat. This is consistent with the idea of the uniformly distributed hot gas in the radiation-dominated universe (section 1.1). In fact, this radiation comes from photons in a last-scattering surface, from the time at which the optical depth became just small enough for the photons to escape (just after recombination). The radiation is highly redshifted, having wavelengths in the order of 1 millimeter, therefore it is called the Cosmic Microwave Background (CMB) radiation. Observations with the COBE satellite in 1992 found the first anisotropies (temperature fluctuations) of 1/1000 in the flat blackbody background of 2.725 Kelvin. Following balloon experiments confirmed this, and very recently the results of the very sensitive WMAP survey were published, which show the spectrum of fluctuations with very high angular resolution (for a comparison of COBE and WMAP, see Figure 1.6)[8].

The fluctuation pattern in the CMB is caused by a set of different physical mechanisms. Since the data from WMAP have a 33 times higher angular resolution than that of COBE (and a 45 times higher sensitivity), the anisotropies detected by both satellites have different origins.

---

[8] `http://lambda.gsfc.nasa.gov/` for both COBE and WMAP

Large scale fluctuations: COBE

The large-scale fluctuation field detected by COBE (with 7° angular resolution) originates from the gravitational potential perturbations at last scattering. The more dense spots have higher redshifts and therefore lower temperatures, since the photons 'climb out' of deeper potential wells. This effect is somewhat lowered by time dilation, causing the temperature to be lower at these denser spots. These fluctuations are called *Sachs-Wolfe fluctuations* (Sachs & Wolfe 1967 [26]), and are dominant for wavelengths $\geq 1h^{-1}$Gpc.

Small scale fluctuations: WMAP

The small-scale fluctuation field as observed by WMAP show the *acoustic peak* of Doppler and adiabatic effects. The Doppler effect is the dynamical effect of the moving plasma scattering the photons, leading to a Doppler shift in frequency and therefore to a different temperature. This effect is quickly dominated by the adiabatic effect: the coupling of matter and radiation can cause compression of radiation in high-density regions, giving a higher temperature at those spots. There is a contradiction in the sense that recombination should always occur at the same temperature and this would rule out the fluctuations, but denser spots recombine later, therefore are less redshifted and appear hotter.

Since these effects can be fully quantitatively analyzed, the observed temperature anisotropy field can be used to reconstruct the initial density field to some scale quite accurately. The density fluctuations are thought to be the origin of the formation of the structure as is observed now. The WMAP survey lead to results like a more accurate estimate for the Hubble constant ($H_0 = 71$ km s^{-1}Mpc^{-1}) and the age of the universe ($t_0 = 13.7$ Gyr), see also Table 1.3.

Table 1.3: Some cosmological parameters as in the best model from the first WMAP data, these values are from table 3 in Bennett et al. (2003) [2].

parameter	value		units
H_0	71	$+4/-3$	km s^{-1}Mpc^{-1}
t_0	13.7	± 0.02	Gyr
Ω_Λ	0.73	± 0.04	
Ω_m	0.27	± 0.04	

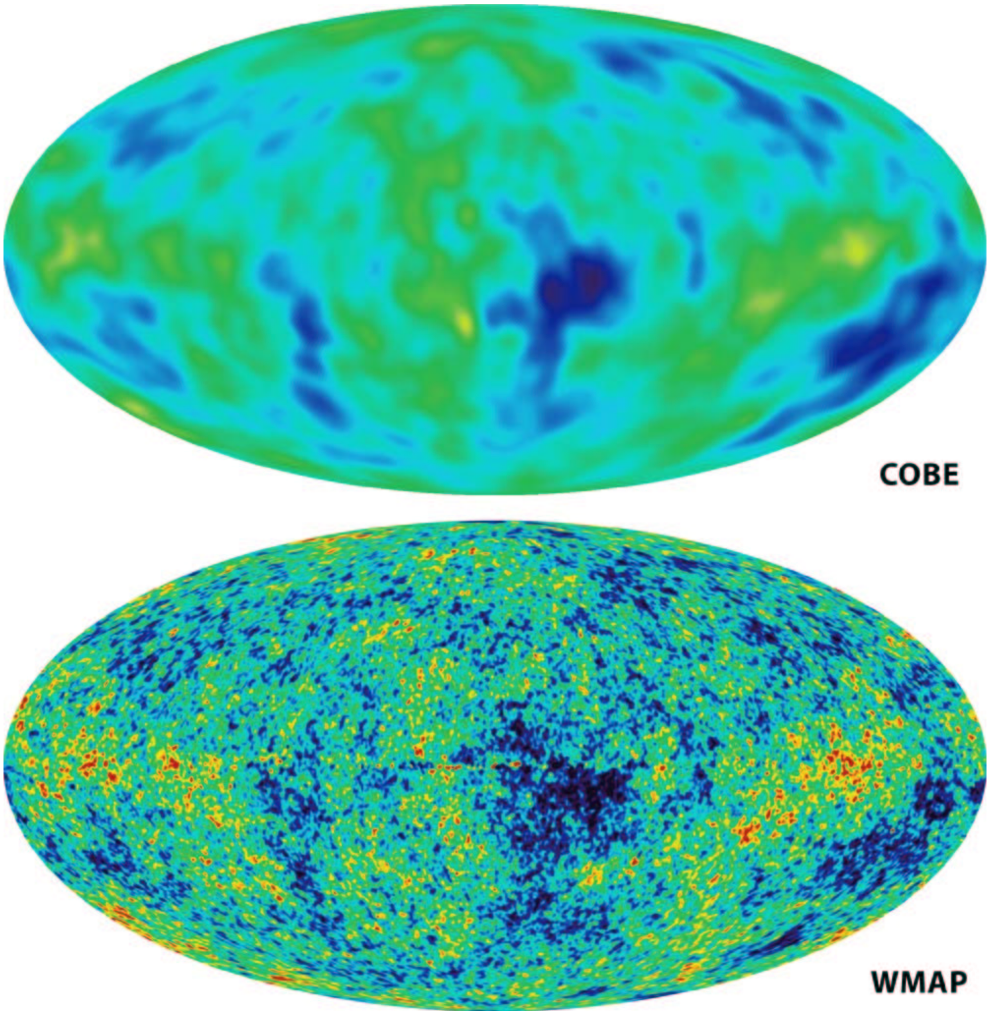

Figure 1.6: Whole sky view of fluctuations. Top: map from COBE (1992) with 7° angular resolution, on this scale dominated by the Sachs-Wolfe fluctuations. Bottom: WMAP (2003) with 13′ angular resolution, on this scale the Doppler and adiabatic effects are visible. Courtesy: NASA/WMAP Science Team.

1.2.3 The peculiar velocity field

According to structure formation theory, the density fluctuations as described in the previous section grew out to the large scale structure as seen in section 1.2.1. Therefore, fluctuations in the velocity field are directly linked to the primordial density fluctuations. Due to these random fluctuations, the total velocity deviates from the expansion velocity. These deviations constitute the *peculiar velocity field*. The major theory is that the initial density fluctuation field grew out to the peculiar velocity field by *gravitional instability*, which is described in the next chapter. If this is true, the observed peculiar velocity field can give us an estimate for the value of the cosmic density parameter Ω. There are several ways to do this, some of which link the velocity field to the density field. The main methods will be treated in the next chapter (section 2.5).

For the measurement of the peculiar velocity of a galaxy, we have to separate the total velocity into the expansion component and the peculiar motion:

$$\mathrm{v}_{gal} = cz = H_0\mathbf{r} + \hat{\mathbf{r}} \cdot [\mathrm{v}_{pec}(\mathbf{r}) - \mathrm{v}_{obs}] \tag{1.13}$$

where v_{gal} is total measured velocity of the galaxy, $\hat{\mathbf{r}}$ is the unit vector towards the galaxy, v_{pec} is the peculiar velocity of the galaxy and v_{obs} is the peculiar velocity of the observer. To measure our own peculiar velocity v_{obs}, the CMB can serve as a rest frame. COBE and WMAP found a dipole in the background radiation, indicating a local flow with a velocity of ~ 600 km/s for our Galaxy together with the cluster of galaxies we are part of, the Local Group. For subtraction of the expansion velocity, there is a need for a distance indicator that is set independently from redshift. Such distance indicators are for example the empirical Tully-Fisher and Faber-Jackson relations, or the measurement of Doppler shifts from Supernova explosions. Unfortunately, those methods are not always applicable and suffer from errors and uncertainties.

It is difficult to describe the observed density and velocity fields, only knowing the mass and velocity at the locations of the galaxies. Therefore, techniques have been developed to reconstruct the continuous density and velocity fields from the observed discrete distributions. One of them is the POTENT reconstruction method by Bertschinger & Dekel [7]. If there is a large number of galaxies in the survey, reconstruction can be done by smoothing the data: compute the average value using some weighting function within some volume for a set of points. Figure 1.7 is an example of a reconstructed field, with velocity vectors and overlaid density contours. This field was derived by Gaussian smoothing from the distribution of IRAS galaxies in the PSCz redshift survey, and shows a section along the Supergalactic plane [8].

Another problem is that the mass of a galaxy has to be estimated from the amount of light that comes from the galaxy, while there is evidence for a substantial dark matter component. This is expressed in terms of the *bias factor* b,

$$\rho_{gal} = b\rho \tag{1.14}$$

where ρ_{gal} is the local measured density of the galaxy and ρ is the 'real' density. As we will see, there exist methods for estimating Ω that circumvent this galaxy mass problem.

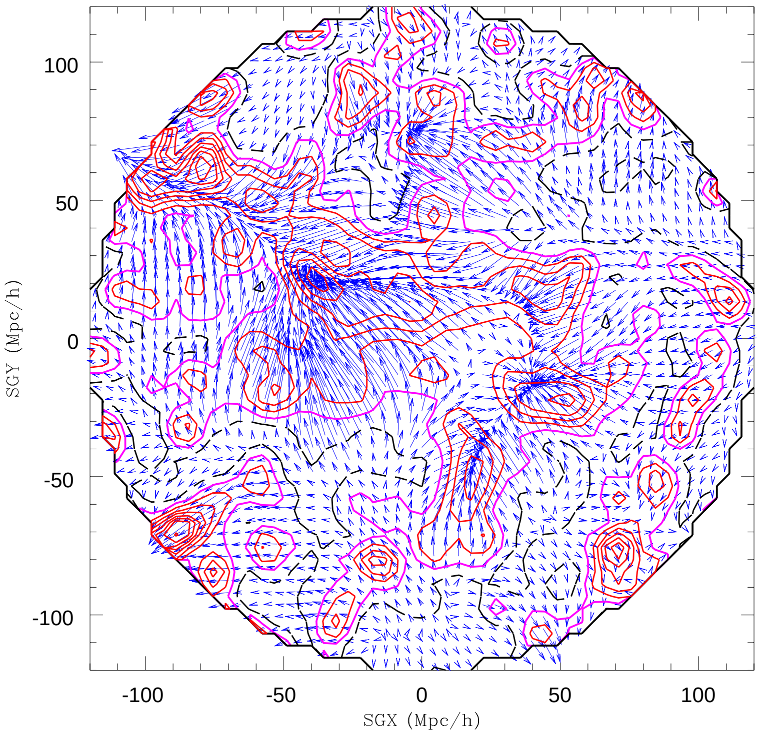

Figure 1.7: The local peculiar velocity field from the infrared PSCz survey. This field was calculated by Gaussian smoothing with a radius R_{sm} of $6h^{-1}$Mpc. The total radius is $120h^{-1}$Mpc. From Branchini et al. 1999 [8].

Chapter 2

Structure formation

Although the overall universe can be described as homogeneous, the observations show that there are detailed features in all directions, ranging from stars and galaxies to galaxy-clusters and the large scale filaments with sizes of about 100 Megaparsec (section 1.2.1). The underlying process responsible for the formation of these structures is not yet fully understood. The existing theories are mainly based on the existence of an original field of very small density fluctuations which grew simply due to gravity as time passed, causing the formation of matter-lumps. The origin of these fluctuations is an issue that is still being discussed nowadays. The two main theories are that of quantum zero-point fluctuations during an inflationary area and the effect of topological defects formed in a cosmological phase transition (chapters 10 and 11 of Peacock 1999 [21]). The characteristic scale of the fluctuations as resulted from the WMAP data favour the inflationary universe, with quantum fluctuations as the origin. The first section of this chapter gives a description of the density fluctuation field, followed by the theory of fluctuation growth in the linear regime (section 2.2) and in the non-linear regime (section 2.3). Section 2.4 explains how structures formed according to clustering models. The last section describes the cosmic velocity field and how it can be traced back to the original density fluctuation field. Generally, most of this chapter can be found in chapters 15 and 16 of Peacock 1999 [21].

2.1 The primordial density field

To make things easier, the fluctuations are defined as a dimensionless density contrast:

$$\delta(\mathbf{r}) \equiv \frac{\rho(\mathbf{r}) - \rho_0}{\rho_0} \tag{2.1}$$

To study the evolution of density perturbations on different scales, the fluctuation field can be decomposed into its spatial components. The best way to do this is by Fourier decomposition:

$$\delta(\mathbf{x}) = \Sigma_k \, \hat{\delta}(\mathbf{k}) \, e^{-i\mathbf{k}\cdot\mathbf{x}} \tag{2.2}$$

$$\mathbf{k} = \frac{2\pi}{\lambda_k} \, \hat{e}_k \tag{2.3}$$

where $\hat{\delta}(\mathbf{k})$ is the amplitude of wave $\mathbf{k}$. This way, small-scale waves and large-scale waves can be distiguished.

The density can be divided in two parts: nonrelativistic matter density and radiation density. These are interrelated, having two distinct perturbation modes: adiabatic perturbations and isocurvature perturbations. For adiabatic perturbations some volume elements are compressed and expanded adiabatically, so both densities change by the same factor. The energy densities, however, have different relations: $\propto T^4$ for radiation and $\propto T^3$ for number density, such that

$$\delta_r = \frac{4\delta_m}{3} \tag{2.4}$$

The opposite are isocurvature perturbations, perturbing only the entropy density and not the energy density. The total density remains homogeneous and there is no perturbation to the spatial curvature:

$$\rho_r \delta_r = -\rho_m \delta_m \tag{2.5}$$

In the very early stages, the isocurvature perturbations are effectively isothermal ($\delta_r = 0$) causing only significant matter density variations. But δ_r becomes negative as δ_m falls. We define $\delta_r = \frac{4}{3}(\delta_m - \delta_i)$, where δ_i is some initial value of δ_m. At late times, $\delta_m \to 0$ and

$$\delta_r \to \frac{-4\delta_i}{3} \tag{2.6}$$

The primordial fluctuation field thus is assumed to be a Gaussian, statistical noise field. As mentioned at the start of this chapter, this is predicted by the inflationary models where the density fluctuations are generated by quantum fluctuations in a scalar field during the inflationary phase. But also generally this is true because of the central limit theorem, which states that data which are influenced by many small and unrelated random effects are approximately normally distributed [27]. This implies adiabatic initial conditions rather than isocurvature perturbations. For statistics of primordial density perturbations, see Peacock & Heavens (1985) [22]. A famous paper on statistics of Gaussian random fields is from Bardeen et al. (1986), also known as BBKS [1].

Assuming these Gaussian initial conditions means that the density contrast δ is a Gaussian random field, described fully by its two-point correlation function, or equivalently by the *power spectrum* $P(k)$, which is the Fourier transform of the correlation function and the square of the Fourier transform of the density contrast

$$P(k) \equiv \langle|\delta_k|^2\rangle \tag{2.7}$$

The power spectrum yields the relative contribution of the full range of fluctuations to the density field:

$$\sigma_0^2 = \int \frac{\mathrm{d}\mathbf{k}}{(2\pi)^3} P(k) \tag{2.8}$$

where σ_0 is the total local density fluctuation:

$$\sigma_0 = \langle\delta(\mathbf{r})^2\rangle \tag{2.9}$$

(the brackets denote it is volume averaged). The correlation function of the density field $\xi(r)$, defined by

$$\xi(r) \equiv \langle\delta(\mathbf{x})\delta(\mathbf{x}+\mathbf{r})\rangle \tag{2.10}$$

is the Fourier transform of the power spectrum:

$$\xi(r) = \xi(|r|) = \int \frac{\mathrm{d}\mathbf{k}}{(2\pi)^3} P(k) e^{-\mathrm{i}\mathbf{k}\cdot\mathbf{r}} \tag{2.11}$$

The correlation function as used for spatial matter distribution is defined as the mean excess number of galaxy pairs at separation r, over that expected for a pure Poisson distribution. For the power spectrum, the correlation function gives a complete statistical description of the density field for a (random) Gaussian field. Higher-order correlations are a measure of non-Gaussianity [32].

2.2 Gravitational instability in the linear regime

The large scale structure of the universe as far as we can see has a foam-like shape, characterized by empty voids, separated by walls, intersecting at elongated filaments that come together in clumps. To understand how structure formation originated from these tiny fluctuations in density, some background information is needed on the theory of gravitational instability. This section treats the linear perturbation theory, which is valid for very small density fluctuations.

General equations

One necessarily has to include the force, gravitation and mass continuity in the expanding universe,

$$\frac{\partial\rho}{\partial t} + \nabla\cdot(\rho\mathbf{v}) = 0 \qquad \text{Continuity equation} \tag{2.12}$$

$$\frac{\partial\mathbf{v}}{\partial t} + (\mathbf{v}\cdot\nabla)\mathbf{v} + \nabla\phi = 0 \qquad \text{Euler equation} \tag{2.13}$$

$$\nabla^2\phi = 4\pi G\rho \qquad \text{Poisson equation} \tag{2.14}$$

so that a description of the mass density field and the velocity field can be made.

Linearized equations

Now assume the fluctuations to be small: $\delta \ll 1$ and use comoving coordinates ($\vec{x}(t) = \frac{\vec{r}}{a(t)}$). Expanding the above equations to first order and subtracting zeroth order solutions, the equations simplify to

$$\frac{\partial \delta}{\partial t} + \frac{1}{a}\nabla \cdot \mathbf{v} = 0 \qquad \text{Continuity equation} \tag{2.15}$$

$$\frac{\partial \mathbf{v}}{\partial t} + \frac{\dot{a}}{a}\mathbf{v} + \frac{1}{a}\nabla \phi = 0 \qquad \text{Euler equation} \tag{2.16}$$

while the Poisson equation remains the same. Combining these equations gives the second-order partial differential equation, the linearized equation for growth of density perturbations:

$$\frac{\partial^2 \delta}{\partial t^2} + \frac{2\dot{a}}{a}\frac{\partial \delta}{\partial t} = 4\pi G \rho_0 \delta \tag{2.17}$$

The assumption of $\delta \ll 1$ implies the assumption that the effect of expansion on the comoving position of the galaxies is negligable. In the very early universe, just after decoupling of radiation and matter at recombination (section 1.1), fluctuations are small and this linear approximation is valid, but in later stages non-linearities will become important and another strategy is needed.

The quasi-linear regime

When δ becomes ~ 1 signs of non-linearity are visible, this is the *quasi-linear* regime. In the quasi-linear regime higher-order Eulerian theory, which is just an extension of linear theory, is applicable. The density contrast δ remains below unity, but the mode-mode coupling between the different Fourier components of δ becomes important, resulting in the build-up of phase correlations. Despite the initial Gaussian field, now non-Gaussian features become important.

2.3 Fluctuations in the non-linear regime

There are two main distinct approaches [33] when $\delta > 1$. The first approach is to choose a few simple configurations and follow their full linear evolution, in order to isolate the most crucial mechanisms. The two main examples are the *homogeneous ellipsoidal model* and the *spherical model.* For a review on non-linear evolution models see Bernardeau et al. (2002) [4].

The second approach is generally to choose a restricted cosmic period or some specific evolution scenarios for which to approximately describe the full matter distribution. This requires conversion of the Eulerian perturbations to a Lagrangian time derivative, which makes it possible to follow a mass element on its path through the evolving cosmic density field. This is useful because it would be too time-consuming to compute the highly accelerating motions on the large timescale that is needed.

Zel'dovich approximation

The most important example of this approach, is the *Zel'dovich approximation* (Zel'dovich, 1970 [37]). This approximation gives a solution for the Lagrangian equations in the case of small density perturbations ($\delta^2 \ll 1$) which is based on the Lagrangian perturbation series of trajectories of mass elements $\mathbf{x}(\mathbf{q}, t)$, truncated at first order. The result is that the displacement of a particle from initial (Lagrangian) comoving position q to Eulerian comoving position x has a simple linear prescription, for which only the initial gravitational potential field is needed:

$$\vec{\mathrm{x}}(\vec{\mathrm{q}}, t) = \vec{\mathrm{q}} - D(t)\nabla\psi(\vec{\mathrm{q}}) \tag{2.18}$$

where $D(t)$ is the growth rate of linear density perturbations and $\psi(\vec{\mathrm{q}})$ is a spatial function, related to the linearly extrapolated potential ϕ by

$$\psi = \frac{2}{3Da^2\Omega H^2}\phi \tag{2.19}$$

Now, the values of δ can be can be calculated by linear extrapolation into the non-linear regime. The strength of the Zel'dovich approximation is that only the initial random field is needed for a qualitative description of nonlinear evolution to the advanced density field.

2.4 Clustering models: top-down and bottom-up

In *top-down* clustering models, large scale waves collapse before the small-scale noise and the matter condensates into clumps. This is what happens in the adiabatic scenario (section 2.1), where galaxies form by fragmentation and the first structures form on a scale of $M \sim 10^{12}$ - $10^{14} M_\odot$ (clusters, superclusters). This is also the case in the Hot Dark Matter model (with collisionless particles having a large range in velocity).

The hierarchical scenario in which small-scale fluctuations collapse first is the *bottom-up* scenario. This is the result of the isothermal scenario, and the first structures form with $M \sim 10^5$ - $10^6 M_\odot$, in a hierarchical way: they cluster to ever larger structures. This results from the Cold Dark Matter, containing collisionless particles with a very small velocity range.

Examples of clustering models

The Zel'dovich approximation in the strong non-linear regime ($\delta > 1$) leads to collapsing into pancakes: the *pancake model.* According to this model, contraction due to a density peak starts in one direction, leading to a higher density, resulting in more contraction in that direction and so on. In three-dimensional space, this results in a flattened structure, the pancake. In the context of the foam, these pancakes represent the walls, intersections are the filaments coming together in clumps (clusters of galaxies) and the spaces in between are the voids (top-down). While matter collapses, the voids simulataniously grow and tend to become more sperical, like in the ellipsoidal model. After this pancake formation, unfortunately, matter keeps on streaming and the pancakes dissolve. Therefore, this method is valid up to the point where matter flows start to cross each other [33]. Extensions are needed, like the *adhesion approximation.* A full review on the Zel'dovich approximation and its extensions is given by Shandarin and Zel'dovich (1989) [30].

Another clustering model is the *hierarchical model* (bottom-up) by Peebles. In this model structures form by the gravitational build-up of small clumps, merging into larger ones. It is now believed that pancakes form generically in models of hierarchical clustering, and the precise size of the pancake is determined by the form of the primordial fluctuation spectrum. Matter in a pancake moves towards the filaments (intersections of pancakes), and matter in filaments moves towards clumps (at intersections of filaments). The period of coexistence of pancakes, filaments and clumps is called the 'cellular epoch'. When most of the matter is in clumps, gravitational instability proceeds hierarchically and neighbouring clumps attract each other, merging to ever more massive clumps [27].

2.5 The cosmic velocity field

The velocity of a galaxy can be divided in two parts; the first is the 'Hubble component', this is the common expansion velocity with which all galaxies move away from each other. The further a galaxy is away, the higher this velocity or 'redshift' is (section 1.1). The remaining part is the *peculiar velocity*, the deviation from the expansion velocity in any direction, having a wide range in size. Assuming the mechanism of structure formation through gravitational instability (section 2.2), we can say that the peculiar velocities of galaxies are induced by the gravitational potential field, originating from the inhomogeneous matter distribution. The exact relation between the velocity field and the matter distribution should be settled by the growth rate of the density fluctuations.

The general linear solution for δ in the second order partial differential equation (2.17) is of the form

$$\delta(\vec{x},t) = A(\vec{x})D_1(t) + B(\vec{x})D_2(t) \tag{2.20}$$

in comoving coordinates, where D_1 and D_2 are the growth factors for the growing mode and the decaying mode respectively. The growing mode is given by

$$D_1(t) = \frac{\dot{a}}{a}\int_0^a \dot{a}^{-3}\mathrm{d}a \tag{2.21}$$

The solutions are defined by the value of the cosmological density, the larger Ω_0, the faster the growth of fluctuations. Later in time, the growing mode will dominate and we can write:

$$\nabla \cdot \mathbf{v} = -a\delta\,\frac{\dot{D}_1}{D_1} = -aH_0 f\delta \tag{2.22}$$

with

$$f \equiv \frac{1}{H_0 D_1}\,\frac{\mathrm{d}D_1}{\mathrm{d}t} = \frac{1}{H_0 D_1}\,\frac{\mathrm{d}D_1}{\mathrm{d}a}\,\frac{\mathrm{d}a}{\mathrm{d}t} = \frac{\mathrm{d}\ln D_1}{\mathrm{d}\ln a} \tag{2.23}$$

Only models with no cosmological constant do have analytic solutions. In the general case there are a couple of approximations for D_1, and therefore for f. A good approximation in linear perturbation theory is $f(\Omega) = \Omega^{0.6}$ by Peebles (1980) [23], where Ω denotes in fact Ω_m. In this approximation the value of the cosmological constant Λ does not heavily affect the growth of fluctuations at low redshifts (Lahav et al. 1991 [18]).

The Poisson equation gives for the peculiar gravitational potential $\phi(\vec{x}, t)$, that is induced by the density perturbations $\delta(\vec{x}, t)$:

$$\nabla^2\phi = \frac{3}{2}\Omega H^2 a^2 \delta(\vec{x}, t) \tag{2.24}$$

$$\phi(\vec{x}, t) = \frac{3\Omega H^2}{8\pi}\, a \int d\vec{x}'\delta(\vec{x}', t)\,\frac{1}{|\vec{x}' - \vec{x}|} \tag{2.25}$$

We can write for the peculiar gravitational acceleration $\vec{g}(\vec{x}, t)$

$$\vec{g}(\vec{x}, t) = -\,\frac{1}{a}\,\vec{\nabla}\phi = -\frac{3\Omega H^2}{8\pi}\int d\vec{x}'\delta(\vec{x}', t)\,\frac{\vec{x}' - \vec{x}}{|\vec{x}' - \vec{x}|^3} \tag{2.26}$$

The peculiar gravitational acceleration in its turn induces *velocity perturbations*, or the peculiar velocity:

$$\mathbf{v}(\vec{x}, t) = \frac{2f(\Omega)}{3H\Omega}\,\vec{g}(\vec{x}, t) \tag{2.27}$$

$$\mathbf{v}(\vec{x}, t) = -\frac{Hf(\Omega)}{4\pi}\int d\vec{x}'\delta(\vec{x}', t)\,\frac{\vec{x}' - \vec{x}}{|\vec{x}' - \vec{x}|^3} \tag{2.28}$$

These formulas were set in comoving coordinates, written in proper coordinates the formula for peculiar velocity is

$$\mathbf{v}(\mathbf{r}) = \frac{H_0 f(\Omega)}{4\pi}\int \mathrm{d}^3\mathbf{r}'\frac{\delta(\mathbf{r}')(\mathbf{r}' - \mathbf{r})}{|\mathbf{r}' - \mathbf{r}|^3} \tag{2.29}$$

where $\mathbf{r} = a(t)\vec{x}(t)$.

The velocity tensors

In the Lagrangian formulation, trajectories of individual particles or fluid elements are followed. In models the position and velocity of a particle, or the density and deformation of a fluid element are defined. The deformation is determined by its differential velocity: its expansion or contraction (velocity divergence), its shear and its rotation (vorticity):

$$\frac{1}{a}\frac{\partial v_i}{\partial x_j} = \frac{1}{3}\theta\delta_{ij} + \sigma_{ij} + \omega_{ij} \tag{2.30}$$

where $i, j = 1, 2, 3$ in three dimensions and δ_{ij} is the delta function (which is 1 for $i = j$, 0 elsewhere). In this formula, the velocity divergence, θ, is the first of the three velocity tensors. The second is the symmetric *shear tensor* σ_{ij}, the third part is the anti-symmetric *vorticity tensor* ω_{ij}. The volume averaged tensors are defined by

$$\theta = \frac{1}{a}\left(\frac{\partial v_x}{\partial x} + \frac{\partial v_y}{\partial y} + \frac{\partial v_z}{\partial z}\right) \qquad \text{divergence} \tag{2.31}$$

$$\sigma_{ij} = \frac{1}{2a}\left(\frac{\partial v_i}{\partial x_j} + \frac{\partial v_j}{\partial x_i}\right) - \frac{1}{3a}\,(\nabla\cdot\mathbf{v})\delta_{ij},\ \sigma_{ij} = \sigma_{ji} \qquad \text{shear} \tag{2.32}$$

$$\omega_{ij} = \frac{1}{2a}\left(\frac{\partial v_i}{\partial x_j} - \frac{\partial v_j}{\partial x_i}\right),\ \omega_{ij} = -\omega_{ji} \qquad \text{vorticity} \tag{2.33}$$

These quantities can be used to compare models to the characteristics of the observed peculiar velocity field.

Cosmological implications of density & velocity fields

This theory of gravitational instability and the implied cosmological parameters therein can help us in putting constraints on those parameters. With improving observations of local density and velocity fields, attempts have been made to measure e.g. the value of Ω. Extensive reviews describing these methods have been written by Dekel (1994) [12] and Strauss & Willick in 1995 [32]. The main methods of obtaining Ω from peculiar velocity fields are shortly described below.

Estimating Ω from the relation between δ and $\mathbf{v}$

We can measure the local density and peculiar velocity field, while we have the theoretical equation 2.29 and the relations between δ and and $\nabla\cdot$ v. Combined with the approximation $f(\Omega) = \Omega^{0.6}$, we can estimate Ω. The theoretical relation between δ and $\nabla\cdot$ v from gravitational instability in the linear regime ($\delta \ll 1$) is, as above (in comoving coordinates):

$$\delta = -\frac{1}{af(\Omega)H}\nabla\cdot\mathbf{v} \tag{2.34}$$

Bernardeau (1992) made an approximation that is based on the statistical (quasi-Gaussian) properties of the matter field [3]. This relation is roughly valid for $\delta \leq 1$, and will become inaccurate when δ is larger than 1 or 2. The result was found to be very close to

$$\delta = \left[1 - \frac{2}{3af(\Omega)H} \nabla \cdot \mathbf{v}\right]^{\frac{3}{2}} - 1 \tag{2.35}$$

One way is to use the velocity of our Local Group as measured from the CMB dipole and to assume that this velocity is induced by mass fluctuations by the formula. When the mass density field is reconstructed from redshift surveys, the value Ω can be calculated. Another way is to combine the reconstructed density and velocity fields and use the linear relation between δ and $\nabla \cdot \mathrm{v}$. In the previous chapter an example was shown of the measured density and peculiar velocity for a field that was reconstructed from redshift survey data.

However, the galaxy bias factor b prevents us from measuring Ω directly. The linear bias model to describe the DM-galaxy discrepancy is

$$\delta_{gal}(\mathbf{r}) = b\delta(\mathbf{r}) \tag{2.36}$$

The assumption is that b is independent of scale of definition of δ. Instead of making a direct estimate for Ω, we can only measure the value of β, with

$$\beta \equiv \frac{f(\Omega)}{b} \tag{2.37}$$

Estimating Ω from isotropy distortions in redshift space

Measuring distortions from isotropy in redshift space in fact gives the velocity divergence field. Therefore, we can obtain δ and $\nabla \cdot \mathrm{v}$ from a redshift survey alone. The measured redshift of a galaxy is changed by its peculiar velocity, but only by the component along the line-of-sight. Since this is in redshift (or comoving) space, we do not need the distance indicators (see section 1.2.3). Using equations 2.34 and 2.35 gives β, because the bias in the redshift surveys still prevents us from measuring Ω when using this method.

Estimating Ω from velocity statistics

Fortunately, there are ways to get around the bias factor. Non-linear effects in the velocity data alone can provide an estimate of Ω independent of b. One way is to determine the deviation from Gaussianity in the probability distribution function (PDF) of the velocity. Another way is to measure the skewness of the velocity divergence distribution θ, which is strongly dependent of Ω_0 [32].

Estimating Ω from velocities in voids

Another way is to use velocities in the voids. In these regions δ is not only small, but also has a firm limit of -1. In linear theory, which is valid because δ is small, δ is proportional to the velocity divergence θ. This implies that θ also has a lower limit, which depends only on the proportionality constant $f(\Omega)$ (equation 2.34). The lowest observed points thus can put a lower limit on Ω, independent of bias. However, the use of this method is susceptible to inaccuracy because reconstructed density/velocity fields are based on values at the galaxy locations. Resolution in low-dense regions is poor, resulting in inaccurate field values just in the voids.

Chapter 3

Computing techniques

Using computer models is one way to test the theory of structure formation and the development of the universe in general. The general idea is to combine a set of 'initial conditions' with a set of theoretical equations and 'see what happens'. The outcome has to be analysed and, if possible, compared to observations. This chapter describes the N-body simulation of large scale structure and the methods for analyzing the results.

3.1 N-body simulations

The N-body simulation is a general method of modelling structure growth in the universe. The idea is to take a number (N) of discrete samples for which to define the initial conditions and to evaluate the equations.

3.1.1 Initial conditions

The initial conditions to be used in the simulation are most crucial. Since the theory states that the large structures in the present emerged from tiny fluctuations in the past, any deviation or missetting of the initial fluctuation field could lead to a totally different universe. Of course, just this fact is interesting as we can learn what initial conditions lead to the universe that is most similar to the real one. Therefore, the starting conditions of the simulation have to be similar to the primordial density field, which is assumed to be of a Gaussian random nature (see section 2.1): at large scale homogeneous with small-scale density peaks. We use an algorithm developed by Van de Weygaert & Bertschinger [35], which elaborates on the Hoffman-Ribak method for defining the initial conditions [16]. Three types of parameters are used to specify the density and velocity at and around the position of the peaks: the scale and position of the peak, the local density field and the local gravitational field. For an extensive description, see Ref. [35]. After setting up these parameters, the Zel'dovich approximation is used for determining the positions and velocities for as far in time as possible, until $\delta \approx 1$. Then, this field can be put into the N-body simulation for the non-linear evolution. With this method, a constrained field containing specified objects can be set up in such a way that the simulation approximates the real world, e.g. the motion of the Local Group (section 4.1).

3.1.2 Force calculation

To get the result that best approximates the natural, continuous universe, as many particles as possible should be used. As there is a limit to the memory and computational power of the computers, programs need to be as efficient as possible. Several methods of force calculation have been developed to reach this. Two important concepts are the Particle-Particle (PP) and the Particle-Mesh (PM) methods [15]. These two and the combined PP/PM, which is used in the project, are described below. Other methods include the *tree codes* and hydronamical methods, e.g. Smoothed Particle Hydrodynamics (SPH).

Particle/Particle (PP)
In PP-calculation, for every single particle in the simulation the gravitational forces by other particles are calculated, which result in a net force and accelaration for this particle. Then, for every particle the new position and velocity can be calculated and set and the next timestep can begin. In a simulation with many particles this becomes extremely timeconsuming, especially for advanced timesteps.

Particle/Mesh (PM)
In the PM-method, the force is calculated to a grid (the mesh), becoming a field quantity. The net force acting on each particle is obtained by interpolation of the mesh-defined values. The advantage is that for each particle only one single calculation has to be made (N calculations), instead of calculations for all particles ($N \times N$ calculations). But this method loses much of accuracy for the short-range forces between particles. To solve part of this problem, a combination of these methods is developed, the Particle/Particle-Particle/Mesh or P3M-method.

Particle/Particle-Particle/Mesh (P3M)
In P3M simulations a combination of Particle/Mesh and Particle/Particle methods is used. For each sample, the direct short-range PP forces are calculated only for particles within a certain distance. This effect is added to the long-range mesh calculated with the PM-method. An improvement of this code is *Adaptive* P3M or AP3M. This method uses finer grids in places of high density only.

The procedure for P3M is as follows:

- start with positions and velocities of the particles
- update the timestep

- calculate PM forces: assign values to mesh, solve for potentials, interpolate forces, change momentum
- calculate PP forces: fill mesh, change momentum
- create equations of motion: update positions, apply boundary conditions, update energies
- integrate to get positions and velocities of the particles

3.2 Pixelization & reconstruction

The N-body simulations work with discrete distributions, and the output is a discrete field: for each particle, the position and velocity are given for the desired time-step. Density and velocity fields from observations are also discrete: the values are only known at the galaxies' positions (Figure 1.7, section 1.2.3). This gives a *mass-averaged* distribution, filtered with function $W_M(\mathbf{x}, \mathbf{x}_0)$

$$f_{mass}(\mathbf{x}_0) \equiv \frac{\int d\mathbf{x}\ f(\mathbf{x})\ \rho(\mathbf{x})\ W_M(\mathbf{x}, \mathbf{x}_0)}{\int d\mathbf{x}\ \rho(\mathbf{x})\ W_M(\mathbf{x}, \mathbf{x}_0)} \tag{3.1}$$

while theoretical predictions, on the other hand, work with *volume-averaged* distributions

$$f_{volume}(\mathbf{x}_0) \equiv \frac{\int d\mathbf{x}\ f(\mathbf{x})\ W_V(\mathbf{x}, \mathbf{x}_0)}{\int d\mathbf{x}\ W_V(\mathbf{x}, \mathbf{x}_0)} \tag{3.2}$$

with $W_V(\mathbf{x}, \mathbf{x}_0)$ as the applied weight function. To be able to compare theory with observations or models, there is a need for the field values at places different from the particle (or galaxy) positions. To achieve this, the discrete distibution has to be interpolated to determine the underlying continuous field. Several interpolation techniques are available for this.

3.2.1 Interpolation on a regular grid

The Nearest Grid Point function (NGP), a first order interpolation method, assigns every particle to the nearest grid point of a static lattice. As a particle moves across a boundary between two grid points, the mass density changes in a discrete fashion. Thus, the mass density is discontinuous.

The Cloud in Cell interpolation method (CIC) is a second order method where not only the nearest, but also the grid point on the other side (1-dimensional!) is taken into account. The nearest grid-point gets weight $(1 - d_{ngp})$, the point on the other side gets weight (d_{ngp}), where d_{ngp} is the distance to the nearest grid-point (in units of cell size). The assigned mass density is continuous but the first derivative is discontinuous.

The Triangular Shaped Cloud method (TSC) is a third order interpolation function. Here three points are included: the nearest grid-point and its two neighbouring points. The nearest grid-point gets weight $(1.75-(\mathrm{d}x)^2)$, the other points get weight $(0.5 \cdot (1.5 - \mathrm{d}x)^2)$, where $\mathrm{d}x$ is the distance from the sample point to the grid point (in units of the cell size). Here both the assigned mass density and its first derivative are continuous but higher order derivatives are discontinuous.

Although the TSC interpolation method does a better job than NGP and CIC, certain circumstances or settings might give some difficulties. When applied to the output-files of N-body simulations which in late stages give a distribution that contains very high-dense regions as well as very low-dense regions, the continuous distribution in the low-dense regions cannot be calculated accurately. Field values in a empty-like region like a void will artificially be zero, therefore it is not efficient to try to zoom into this specific part of the region There is a need for a interpolation method that can do better also in the regions of low-density. The solution is to leave the regular-grid based functions. A good mathematical method is the 'Voronoi tessellation' which is based on the particle positions themselves instead of a regular grid. Its complement is the 'Delaunay tessellation', which will be used in this project.

3.2.2 Voronoi and Delaunay Tessellations

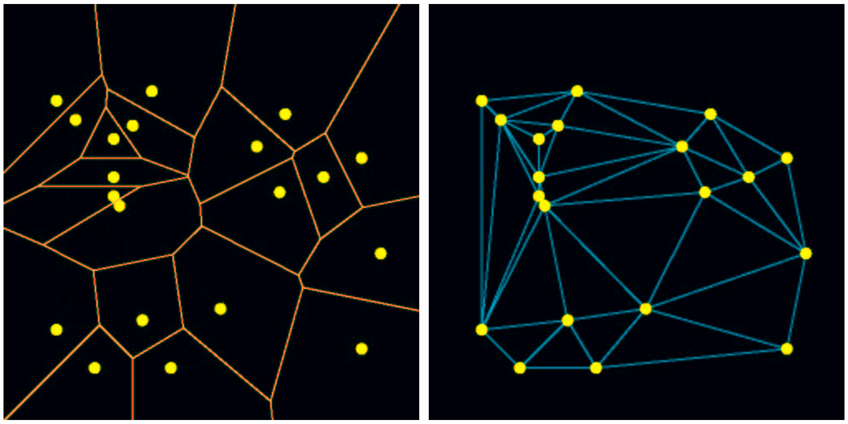

Figure 3.1: The two-dimensional Voronoi tessellation (left) and Delaunay Tessellation (right) of the same point distribution. The voronoi tessellation consists of the exact intersecting lines between any two points, the two dimensional Delaunay tessellation makes triangles by connecting every point with its 2 nearest neighbours. NB: in 3-dimensional space *tetrahedrons* are created by connecting every point with its 3 neighbours.

Voronoi tessellations

A Voronoi tessellation of a point distribution produces cells and vertices. Each point of the distribution is the nucleus of a Voronoi cell. The vortices are the joining points of the cells. The Voronoi distribution is defined by the midway intersecting lines between two neighbouring points (nuclei), see Figure 3.1 (left). All the points inside a Voronoi cell Π_i are closer to the cell's nucleus than to any other:

$$\Pi_i = \{\vec{x} | d(\vec{x}, \vec{x_i}) < d(\vec{x}, \vec{x_j}),\ \forall\, j \neq i\}\,, \tag{3.3}$$

where $\vec{x_j}$ is the position vector of nucleus j and $d(\vec{x}, \vec{y})$ the distance between $\vec{x}$ and $\vec{y}$.

When this is applied to the discrete fields either from observations or N-body simulations, the galaxies or particles are the nuclei of the Voronoi tessellation. From N-body simulations, the velocity and density (or any field value) inside a Voronoi cell is identical to that of its nucleus thus only changing within the walls and filaments: the skeleton structure.

The Voronoi model of large-scale structure

An application of the Voronoi tessellation has been in describing the large scale cosmic matter distribution. The large-scale structure with voids, clusters and superclusters is represented as a geometrical skeleton of walls, filaments and nodes: the Voronoi foam. Physically, this is based on the observation that voids expand faster than surrounding material, resulting in matter flowing out of the voids, into the walls. Once in the wall, the matter tends to flow towards the denser regions: to the filaments, and from the filaments to the nodes. The first practical three-dimensional model was the Voronoi Kinematic model, constructed by Van de Weygaert and Icke in 1989 [36]. Note that the Voronoi nuclei are situated in the large-scale empty voids, therefore one can think of dynamical void evolution as a physical basis for this model.

Delaunay tessellations

The Delaunay tessellation of a point distribution consists of tetrahedrons which are defined by connecting every point with its 3 closest neighbouring points of the distribution, see Figure 3.1 (right). A Delaunay nucleus is defined as the centre of the sphere that circumscribes the cell. The Delaunay and Voronoi tessellations are complementary in the sense that they can be derived from each other: each Delaunay vertex is a Voronoi nucleus, and a Delaunay nucleus is the vertex of the four Voronoi cells whose nuclei are the four points defining this Delaunay tetrahedron.

The Delaunay Tesselation Field Estimator (DTFE)

The Delaunay Tessellation Field Estimator is the application of the Delaunay tessellation method to the discrete outcome of N-body simulations. When the

Delaunay tessellation of a N-body simulation particle distribution is made, the Delaunay vertices are the particles. Therefore, the field value is known for the 4 points that define the Delaunay cell, and the gradient (which is constant within the cell) can be calculated from those four values. Now, the field value at every spot of the tessellated space can be derived via linear interpolation. The field can now be displayed as if it were from a continuous distribution.

DTFE density and velocity fields

The field value f (e.g. velocity) at a particular spot $\mathbf{r}$ inside a three-dimensional Delaunay cell, defined by the vertex points $\mathbf{r}_0, \mathbf{r}_1, \mathbf{r}_2, \mathbf{r}_3$, can be calculated by simple linear interpolation:

$$f(\mathbf{r}) = \alpha_0 f(\mathbf{r}_0) + \alpha_1 f(\mathbf{r}_1) + \alpha_2 f(\mathbf{r}_2) + \alpha_3 f(\mathbf{r}_3) \tag{3.4}$$

where $f(\mathbf{r}_n)$ is the field value at vertex $\mathbf{r}_n$ and α_n is determined by the proportional distance from the point $\mathbf{r}$ to the vertex $\mathbf{r}_n$, with $\Sigma\alpha_n = 1$. Also the nine components of the velocity gradient tensor $\frac{\partial v_i}{\partial x_j}$ can be determined, which are constant within each cell. This results in an easy calculation of values for the velocity divergence, shear and vorticity at any spot inside the cell. The calculation of the velocity gradient of a Delaunay cell is described in detail in Appendix A.

Bernardeau & Van de Weygaert already described this method in 1996 [5]. In fact, they compared the performance of the Voronoi and Delaunay methods (which both produce volume-averaged fields) for this purpose and found the latter to do better in reproducing analytical predictions of e.g. the velocity divergence Probability Distribution Function. When compared to other methods, DTFE does very well in reconstructing cosmic density and velocity fields. A very high resolution can be reached without losing any information, because of the ability to calculate the field values at every location in space. This superior performance is shown for cosmic density and velocity fields from N-body simulatons by Schaap & Van de Weygaert (2000 and 2001) [28, 29]. Bernardeau et al. (1997) and Van de Weygaert & Bernardeau (1998) show how Ω can be obtained from the velocity divergence distribution using Voronoi and Delaunay tesselations applied to N-body simulations [6, 34]. This method is described in section 2.5.

Figure 3.2 shows the DTFE permance compared to TSC[1]. Figure 3.3 is an example of DTFE reconstruction. Compare the real 2dF (south) galaxy distribution (left) with the reconstruction (right)[2].

---

[1] `http://www.astro.rug.nl/ wschaap/dtfe/simulation.html`

[2] `http://www.astro.rug.nl/ wschaap/dtfe/galaxydistr.html`

particles: DTFE: TSC:

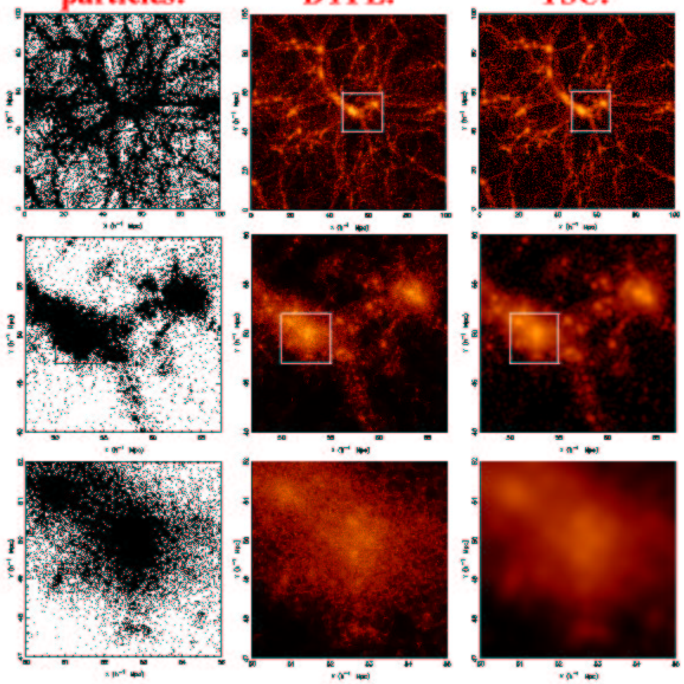

Figure 3.2: Comparison of TSC and Delaunay analysis of an N-body simulation. From top to bottom is zoomed on a particular clump. The left panel shows the particle distribution, the middle and right panels are the TSC and DTFE reconstructions, respectively. This shows clearly the better resolution of DTFE. Courtesy: Willem Schaap.

2dF redshift survey south

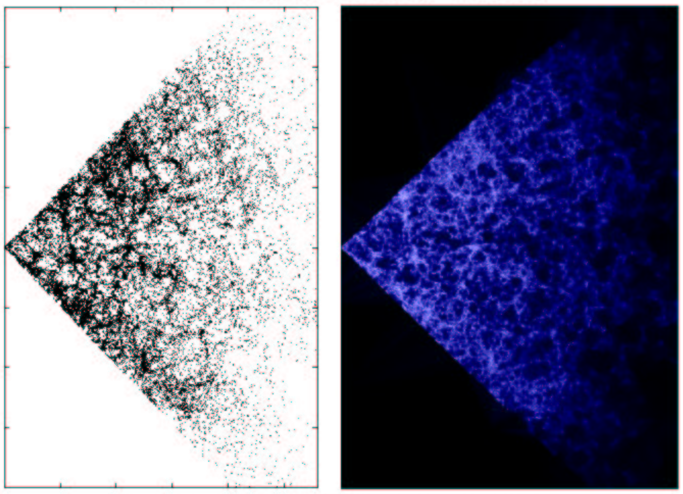

(data taken by the 2dF redshift consortium)

Figure 3.3: The 2dF galaxy redshift survey (left) and DTFE reconstruction (right). Courtesy: Willem Schaap.

Chapter 4

The peculiar velocity field: comparing TSC and DTFE

The aim of this project was to compare the TSC and Delaunay interpolation methods. For this purpose I got the output data from a N-body simulation of large scale structure and I used both methods for calculating the field values. The data was smoothed with three different smoothing radii in order to see the effects on different scales. Several quantities like density and velocity were plotted in several ways to show the results.

4.1 Details of the N-body simulation

The simulation used was a constrained realization of the local universe, using a ΛCDM cosmological model with $\Omega_m = 0.3$, $\Omega_\Lambda = 0.7$, and $H_0 = 70$ km/s/Mpc. The boxsize of this simulation was 320 h^{-1}Mpc, containing 128^3 particles. The simulation was a dark matter simulation performed with a code called HYDRA, which is a combination of AP3M and SPH (section 3.1). Forces were computed on a 256^3 TSC-grid.

In order to limit computing times, I used only a sub-box of $80^3 h^{-1}$Mpc, with its center coinciding with the center of the large simulation box. This volume was still large enough to be able to see large-scale structures and compare the two methods. Besides, the DTFE procedure can best be used on a smaller number of particles since is not efficient enough (yet) in manipulating computing memory. Output was given for ten timesteps with expansion factors a_{exp} of $0.1, 0.2, \ldots, 1.0$. Figure 4.1 shows the particle distribution in the cube for expansion factors 0.1, 0.6 and 1.0.

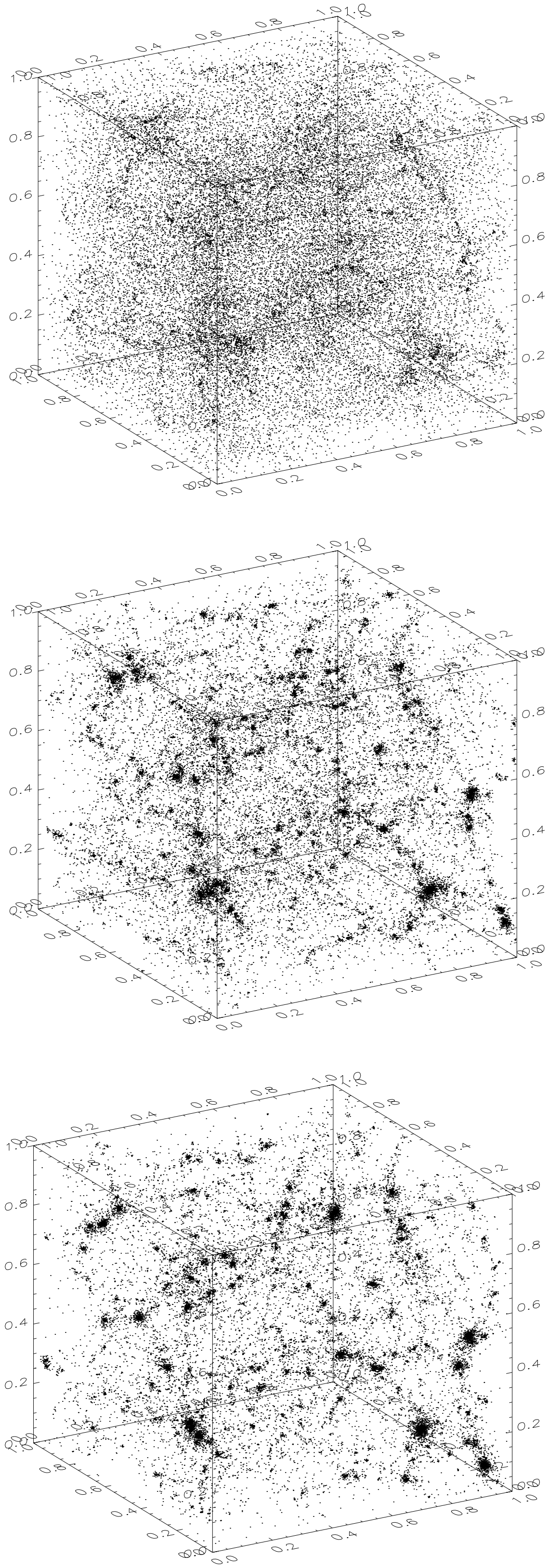

Figure 4.1: Whole 80^3 h^{-1}Mpc N-body cube with particles of the used simulation for different timesteps. From top to bottom: a_{exp} = 0.1, 0.6, 1.0

4.2 The used TSC and Delaunay methods

For computing the values with the TSC-method I used the TSC algorithm of IDL. The densities were calculated by adding up all contributions of particles, whereas the velocities were averaged at the gridpoints. For calculation the velocity derivatives I wrote a code that used a numerical approximation. The sub-box contained about 32000 particles (this number was not the same for each timestep, because particles from the large box move in and out of the small box). Therefore the TSC-grid on which field values were calculated had to contain about this number of cells. Otherwise, the results would be affected by undersampling or oversampling. I computed TSC-values on a grid of $32^3 = 32768$ points.

The used Delaunay tessellation algorithm is an extension for peculiar velocities of the DTFE code (vdWeygaert & Schaap) by Romano-Díaz and Schaap, based on the original code used by Bernardeau & Van de Weyageart 1996 [5]). The code is explained in Chapter 5 of Romano-Díaz 2004 [25]. The DTFE data was computed on a 64^3 grid. At these gridpoints the densities, velocities and partial velocity derivatives were calculated. The files containing these values were povided by Romano-Díaz.

4.3 Displaying the data

Top-hat smoothing

To study the effects on different spatial scales, the data has to be smoothed. It would have been convenient to use a Gaussian filter for smoothing because this can be done in Fourier space, which saves much of computing time. However, this assumes periodic data and since the data came from a sub-box of the original simulation cube, is was not periodic and would give a problem with the edges. For this reason I used top-hat smoothing instead, which is a sphere of uniform weight. The code for top-hat smoothing was written in IDL.

The 'unsmoothed' data (on the grid) had a seperation of $80/64 = 1.25\ h^{-1}$Mpc for DTFE and $80/32 = 2.5\ h^{-1}$Mpc for TSC. Therefore, there's no sense in smoothing on scales smaller than these values. This immediately shows the shortcoming of TSC: the smallest scale is set by the number of particles and the size of the box. The data was smoothed with smoothing radii $R_{\rm sm}$ of 2, 5 and 10 h^{-1}Mpc. The values were calculated for the points of a 20^3 grid, this is because the top-hat smoothing procedure is extremely time-consuming. The eventual grid was even smaller: the outer points were left out because the smoothing spheres should not get over the box-edges.

Resulting figures

To show an overview of the time evolution on different scales, I put these plots into one figure. In the resulting pictures the horizontal evolution is scale evolution, from left to right the sequence is smoothed with R_{th}: **unsmoothed, 2, 5, 10** h^{-1}Mpc. Sometimes the 'unsmoothed' column has been left out. This is because it is only useful for DTFE, since for TSC this is almost the same as the data smoothed with $R_{th} = 2$ Mpc because of the difference in resolution. The vertical evolution is in time, with from top to bottom the expansion factors a_{exp} of **0.1, 0.2, 0.3, ... , 1.0**.

Contour plots & vector plots

Figures 4.3 and 4.4 show contour plots of δ in the middle x-plane for TSC and DTFE respectively. The contour levels are the same in both figures. Vertically is the time evolution, the horizontal evolution is in scale as described above. The velocity vector plots of the same slice are shown in Figures 4.5 (TSC) and 4.6 (DTFE). Note that the unsmoothed values could be calculated on a 64×64 grid for DTFE, while for TSC this resolution gives an errornous result. The contourplots of unsmoothed data on a 64x64 grid for both TSC and DTFE are shown below in Figure 4.2.

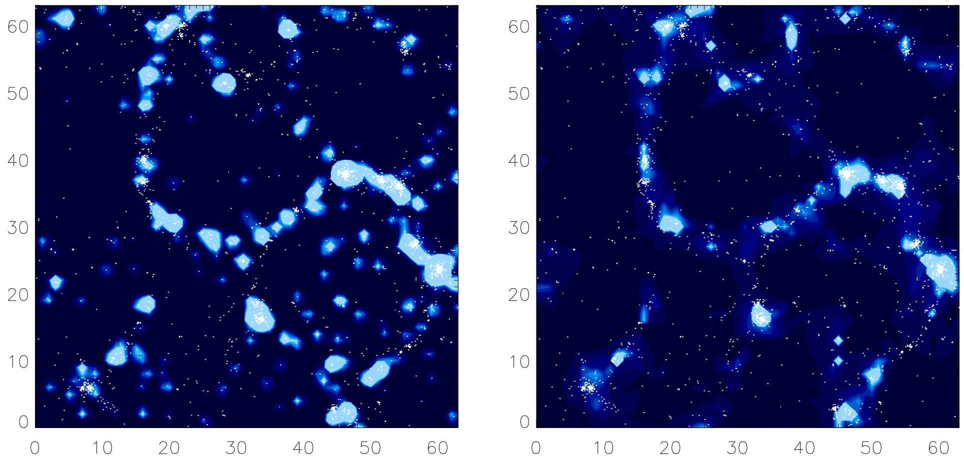

Figure 4.2: Contourplots on a 64x64 grid for TSC (left) and DTFE (right), along x-plane in the middle of the cube. TSC creates large differences between low-dense and high-dense regions. DTFE contours show a more smooth approximation of the density field.

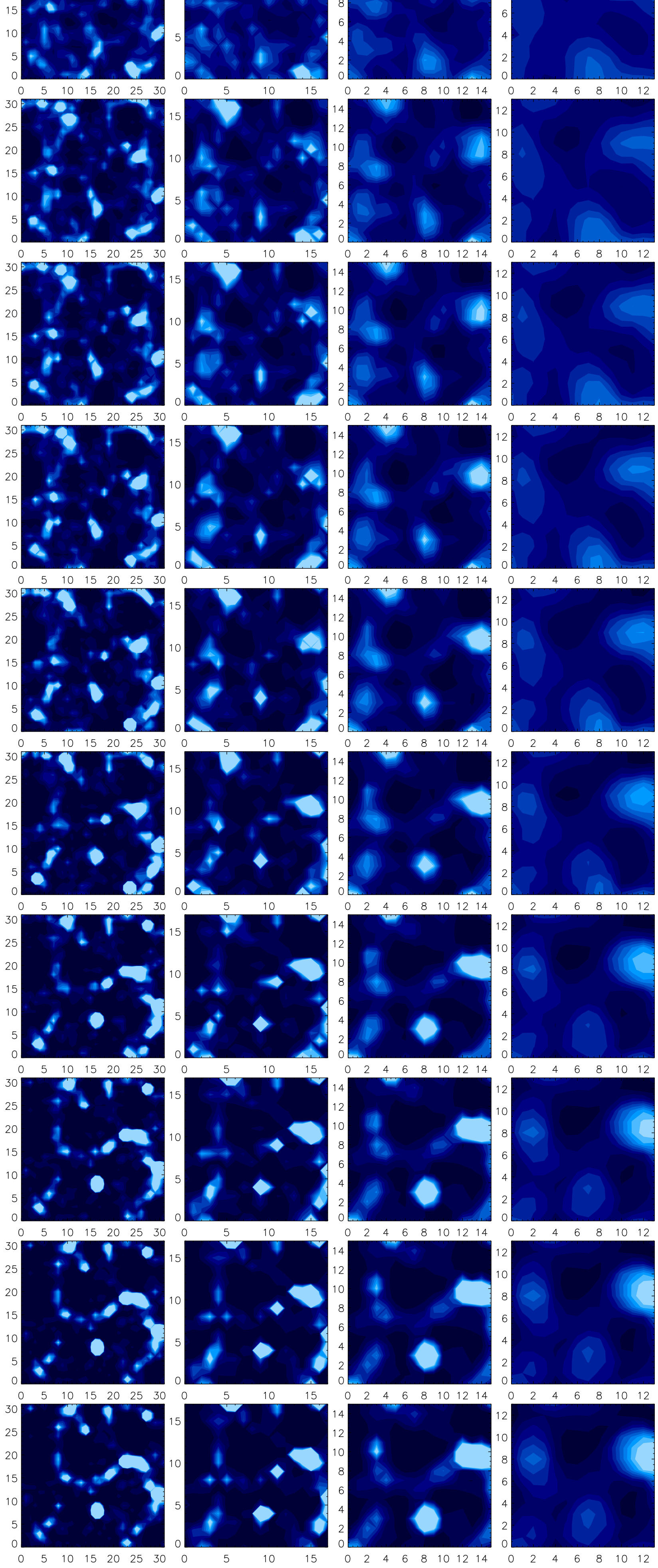

Figure 4.3: Contour plot TSC density (δ) along middle x-plane. The larger the scale (R_{sm}), the further inwards the plot-region (see text).

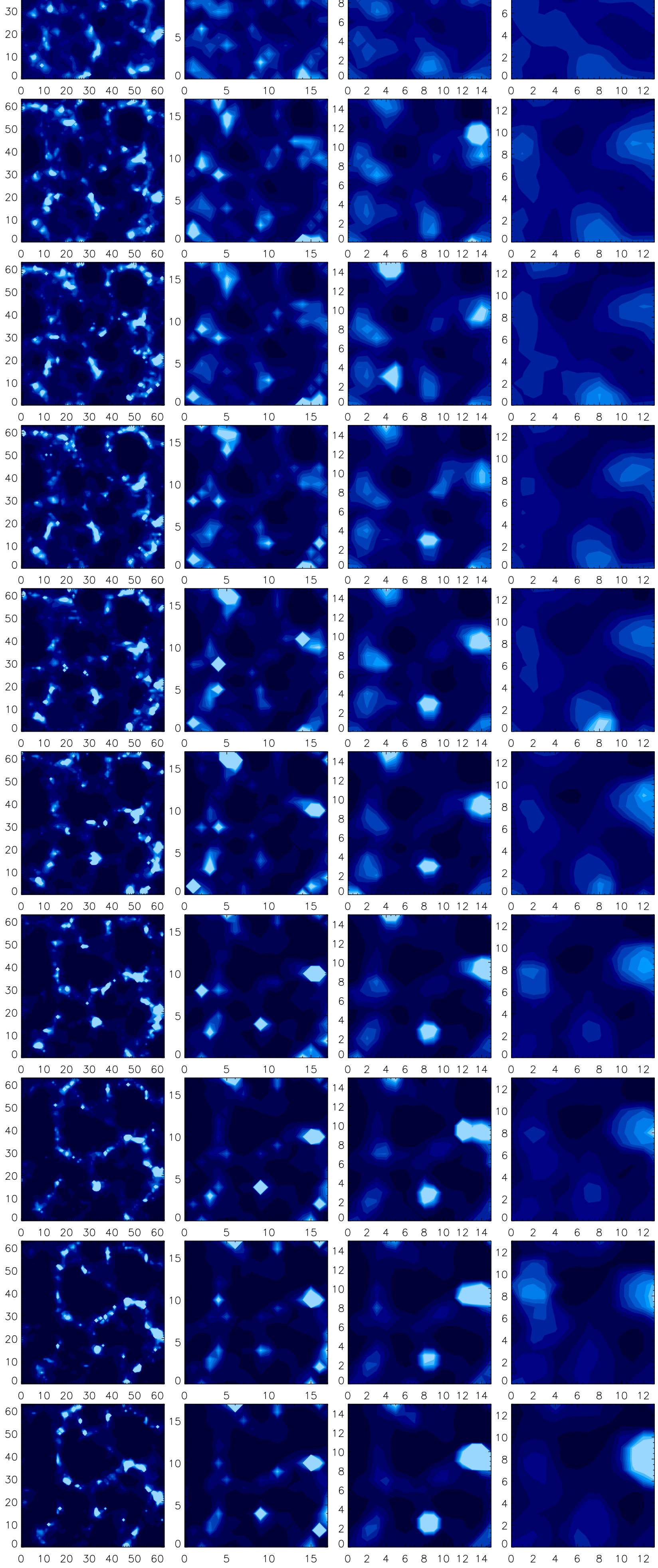

Figure 4.4: Contourplot DTFE density (δ) along middle x-plane.

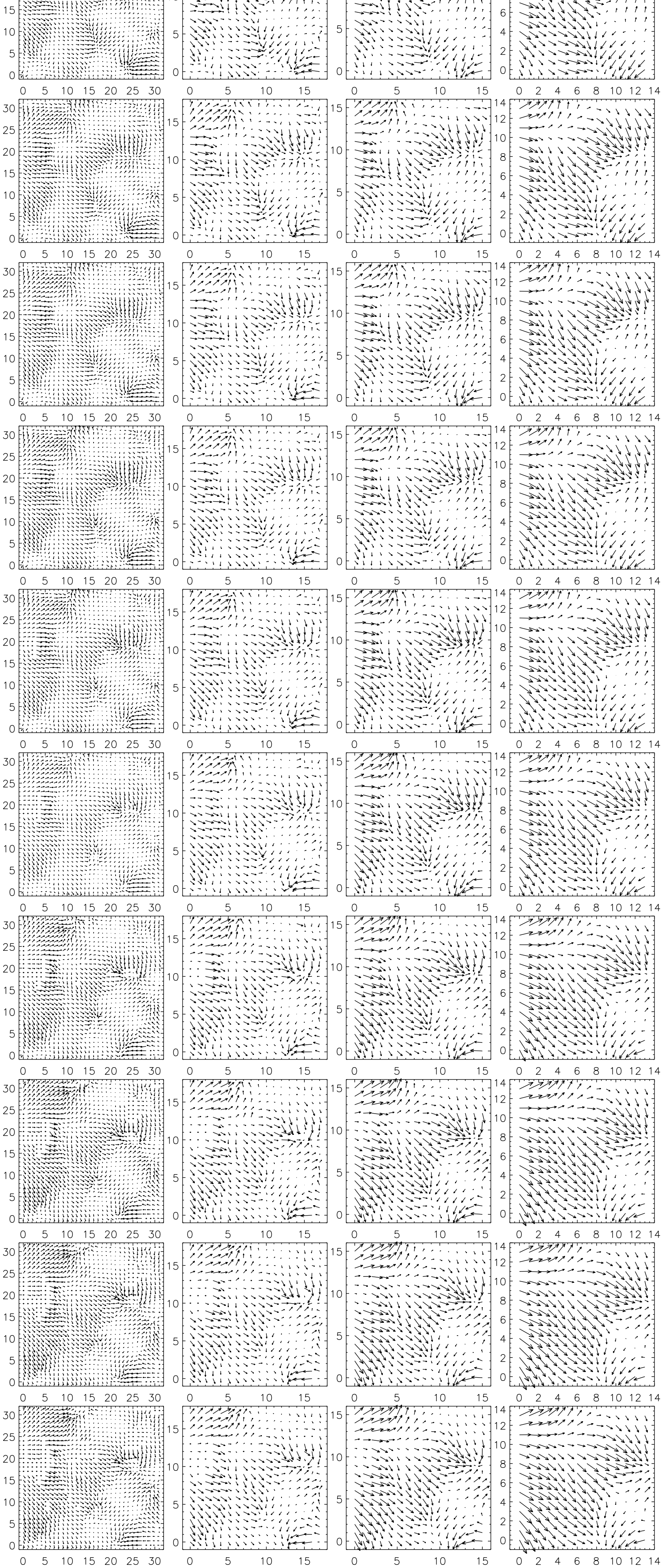

Figure 4.5: Vector plot of TSC velocity vectors along middle x-plane. As with the contour plots: the larger the scale (R_{sm}), the further inwards the plot-region (see text).

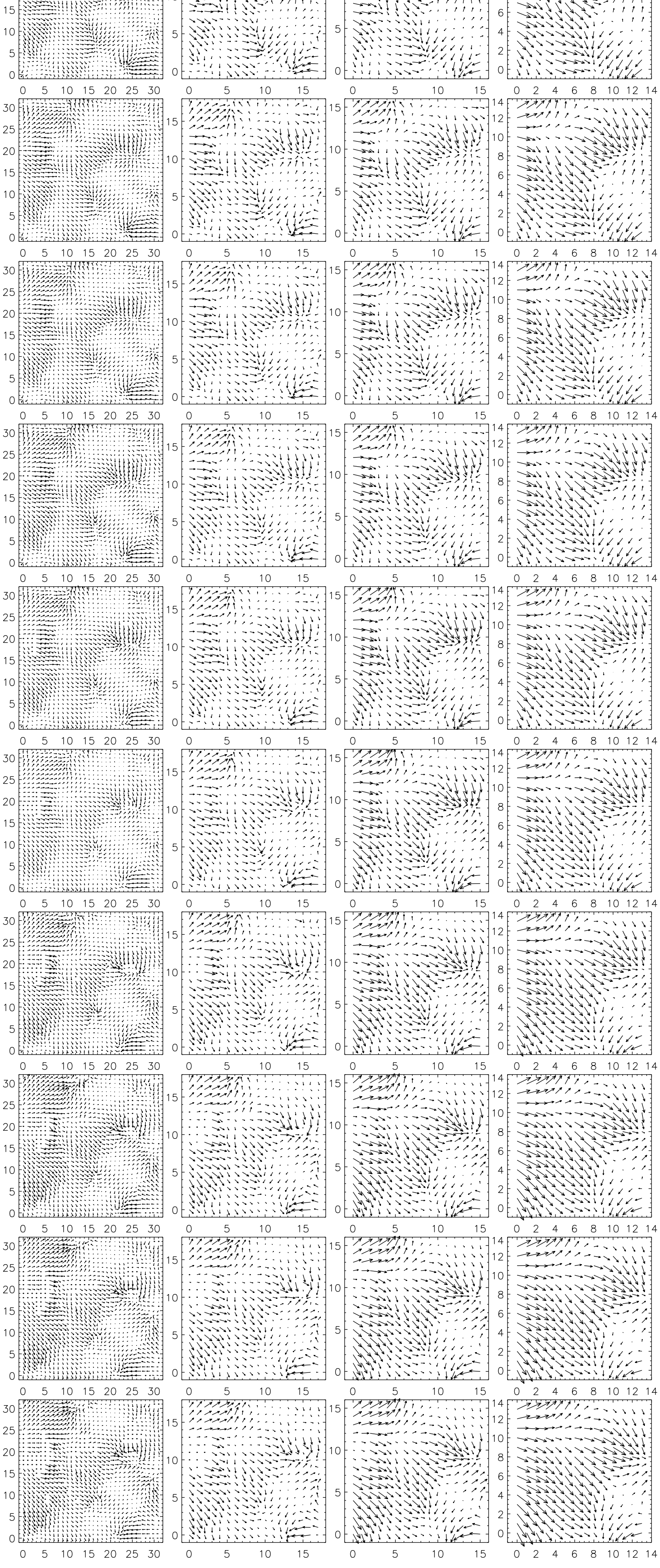

Figure 4.6: Vector plot of DTFE velocity vectors along middle x-plane.

Scatterplots of DTFE vs TSC

The field values of TSC and DTFE can be directly compared by putting the computed grid values together in a scatter plot. The result is in Figure 4.8 for the densities δ (left) and for the velocities (right), velocity divergence in Figure 4.9. The deviation from the one-to-one relation (dashed line) is much larger for the densities than for the velocities. On larger scales, the values of TSC and DTFE lie closer together. On the other hand, there is no sign of time evolution. There seem to be strange scatter-points in the DTFE values, this could be due to boundary-effects: periodic data is assumed for DTFE, while the data used is not periodic. Also, the performance of DTFE is known to be less accurate in very high-dense regions.

Distributions in histogram plots

Distributions for δ, v and $\nabla \cdot \mathrm{v}$ are shown in histogram-format in Figures 4.10 to 4.13. Each histogram has 25 bins specified for a specific range. Differences between the distributions of TSC and DTFE are clearly seen for δ. At late timesteps, the unsmoothed TSC values are for a major part first bin (Figure 4.7). This is because of the shot-noise. An evolving universe becomes less homogeneous because of the formation of matter-clumps, leaving empty spaces in between. Large regions in the N-body simulation thus contain few or no particles. The values of the TSC grid-points in those regions are set to zero, so a lot of those grid-points contain no information. When the smoothing scale is large, however, this effect is ruled out. The DTFE method does not suffer from this effect.

In all of the figures the time evolution is seen as the distributions evolve from Gausssian to non-Gaussian. The distributions of the velocity divergence are in Figures 4.12 and 4.13. As mentioned before, the deviation from Gaussianity or skewness of the distribution function of $\nabla \cdot \mathrm{v}$ can be used in estimating the value of Ω (section 2.5).

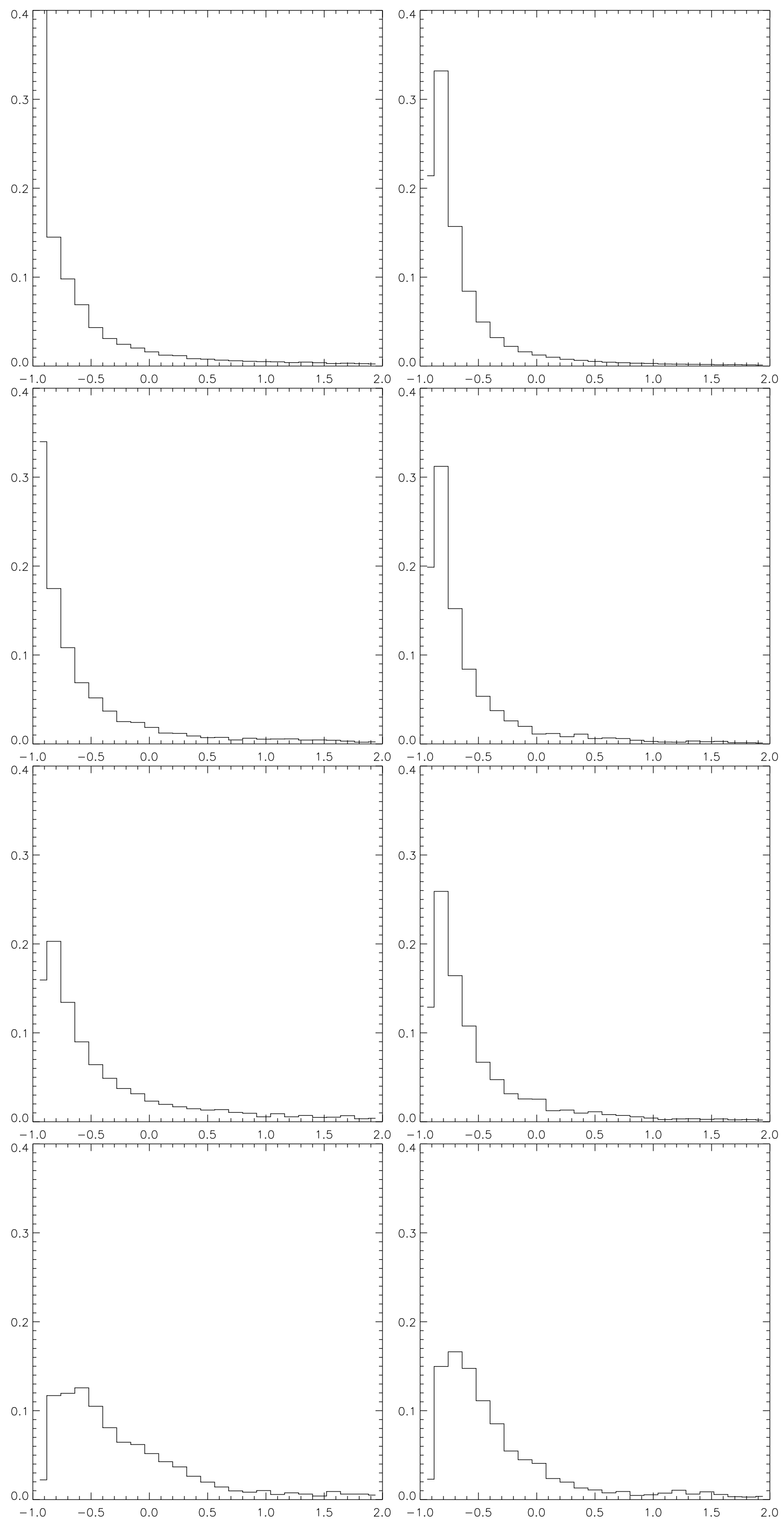

Figure 4.7: Histogram plots of δ values at last timestep. From top to bottom: unsmoothed, 2, 5 and 10 Mpc. Left: TSC, right: DTFE. Note that the unsmoothed values of TSC are for a large part in the first bin, this effect averages out on larger smooth-scales.

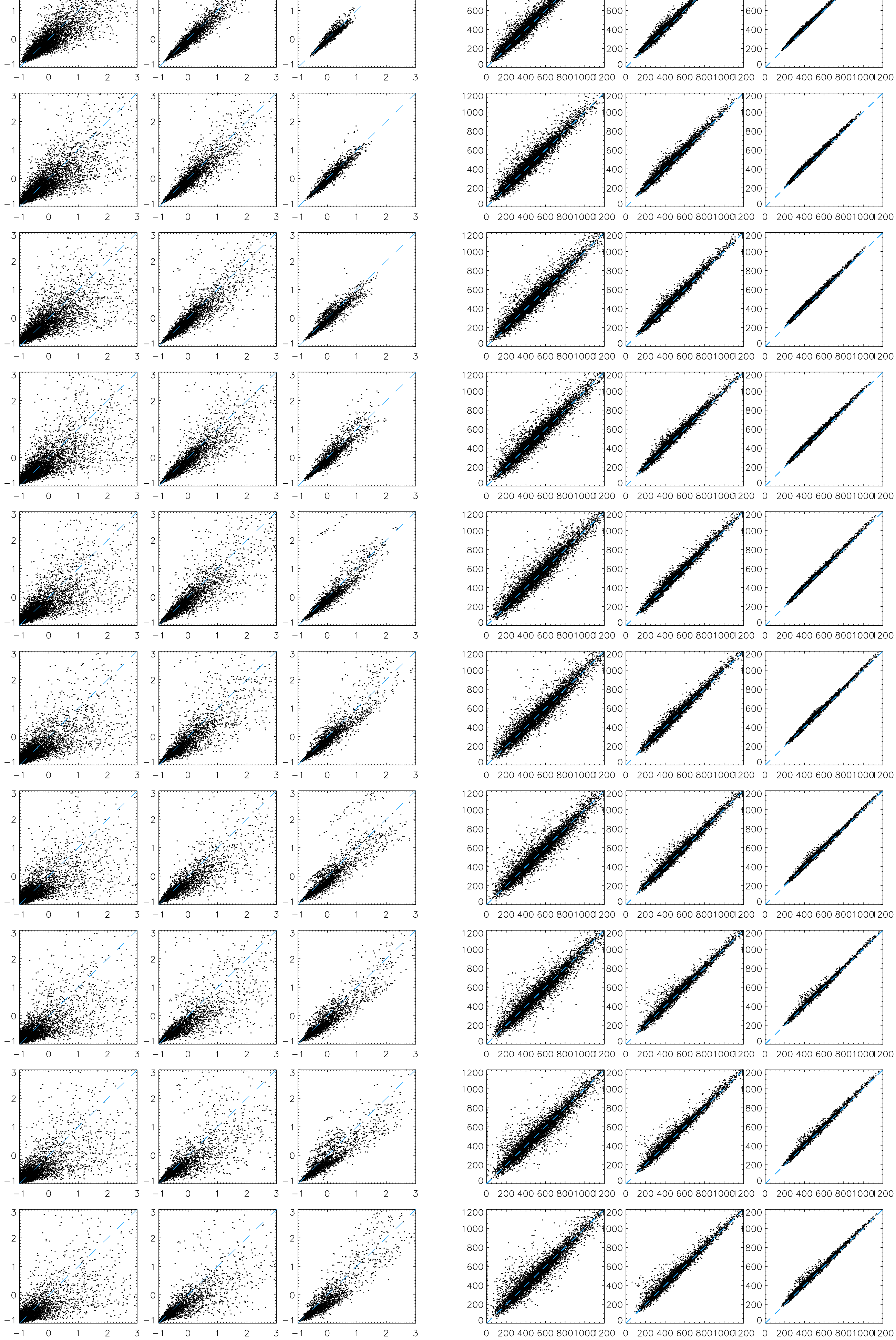

Figure 4.8: Scatter plot of DTFE values (vertical axis) against TSC values (horizontal axis). Left three columns: δ; Right three colums: velocity.

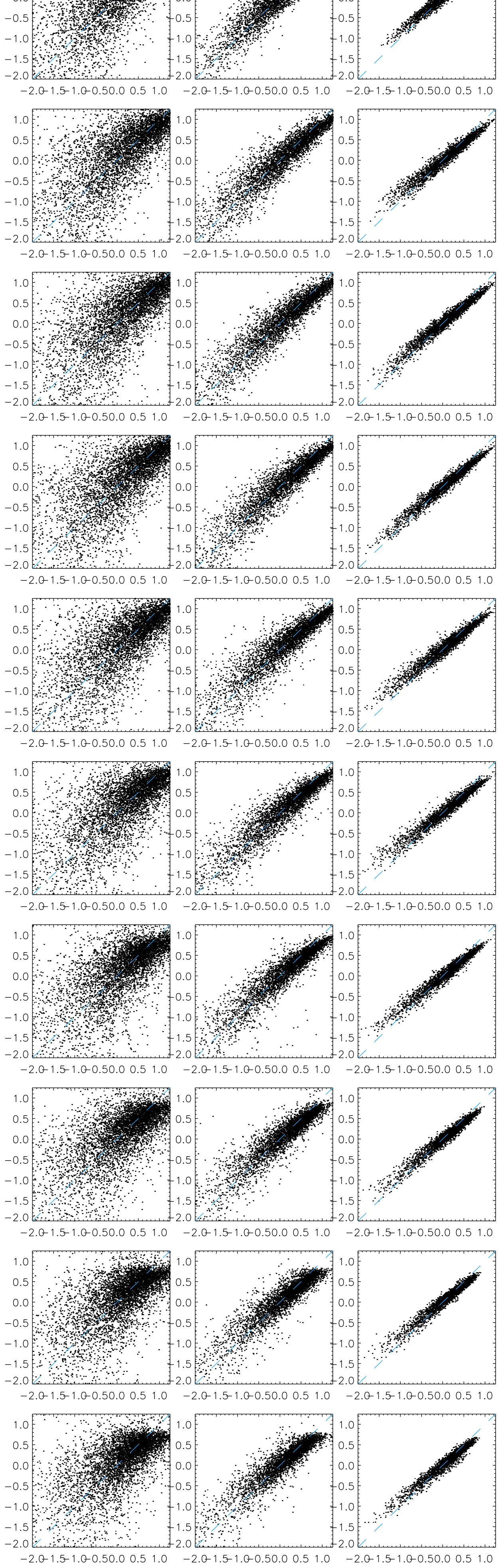

Figure 4.9: Scatter plot of the velocity divergence, each plot shows the DTFE values against the TSC values.

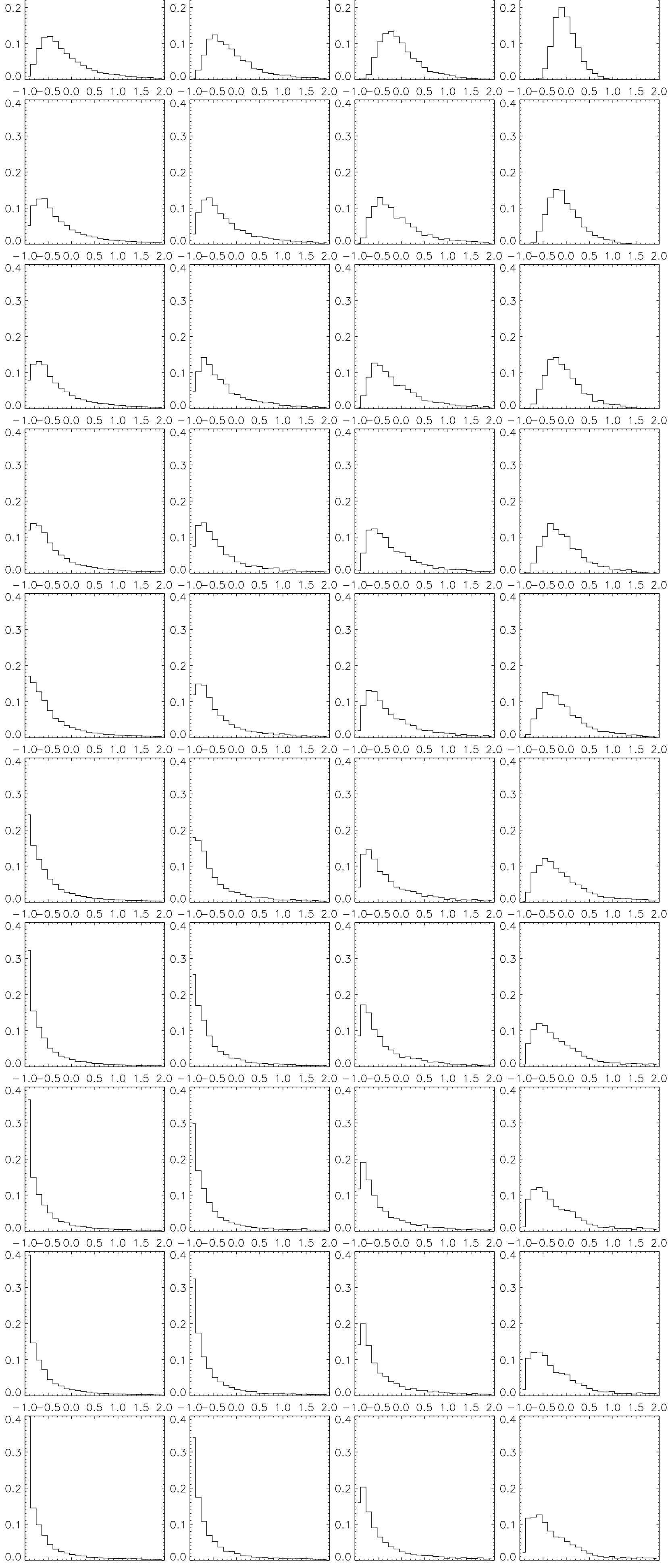

Figure 4.10: Histogram plot TSC density (δ).

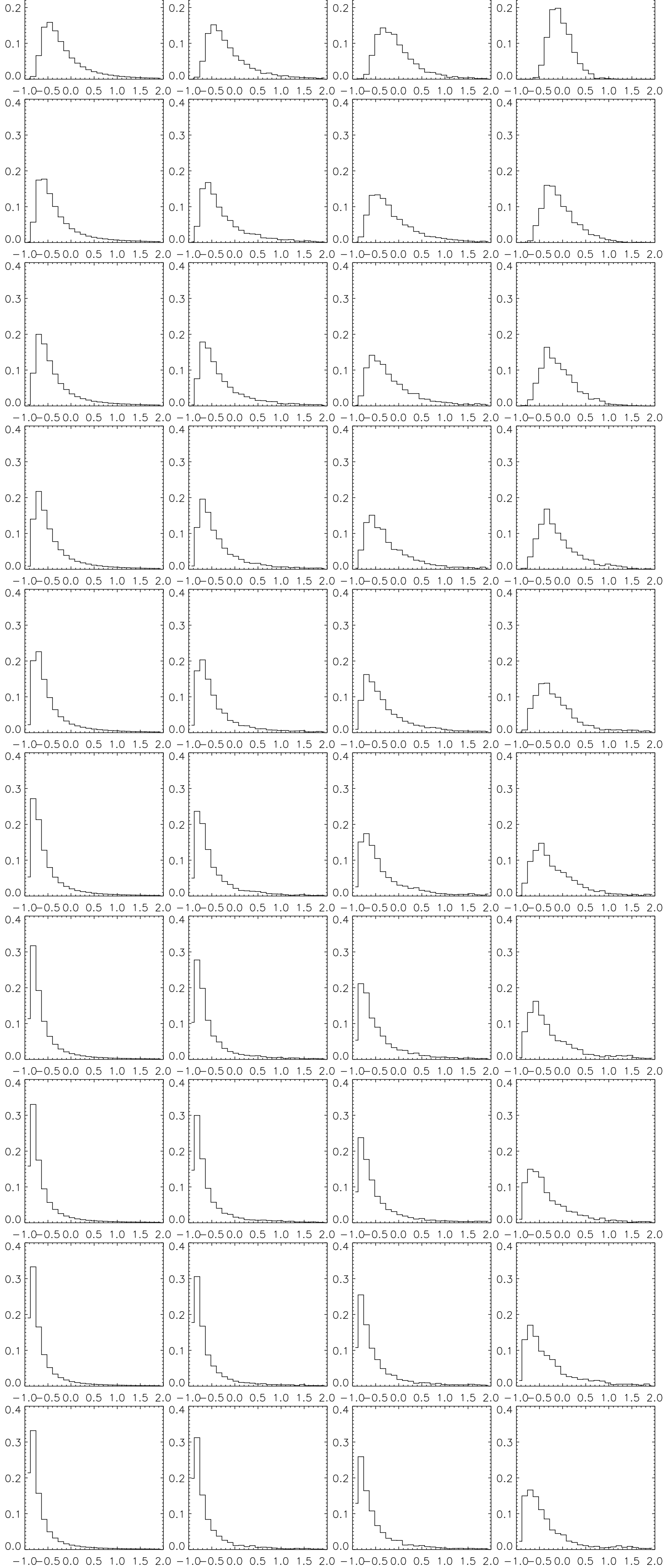

Figure 4.11: Histogram plots DTFE density (δ).

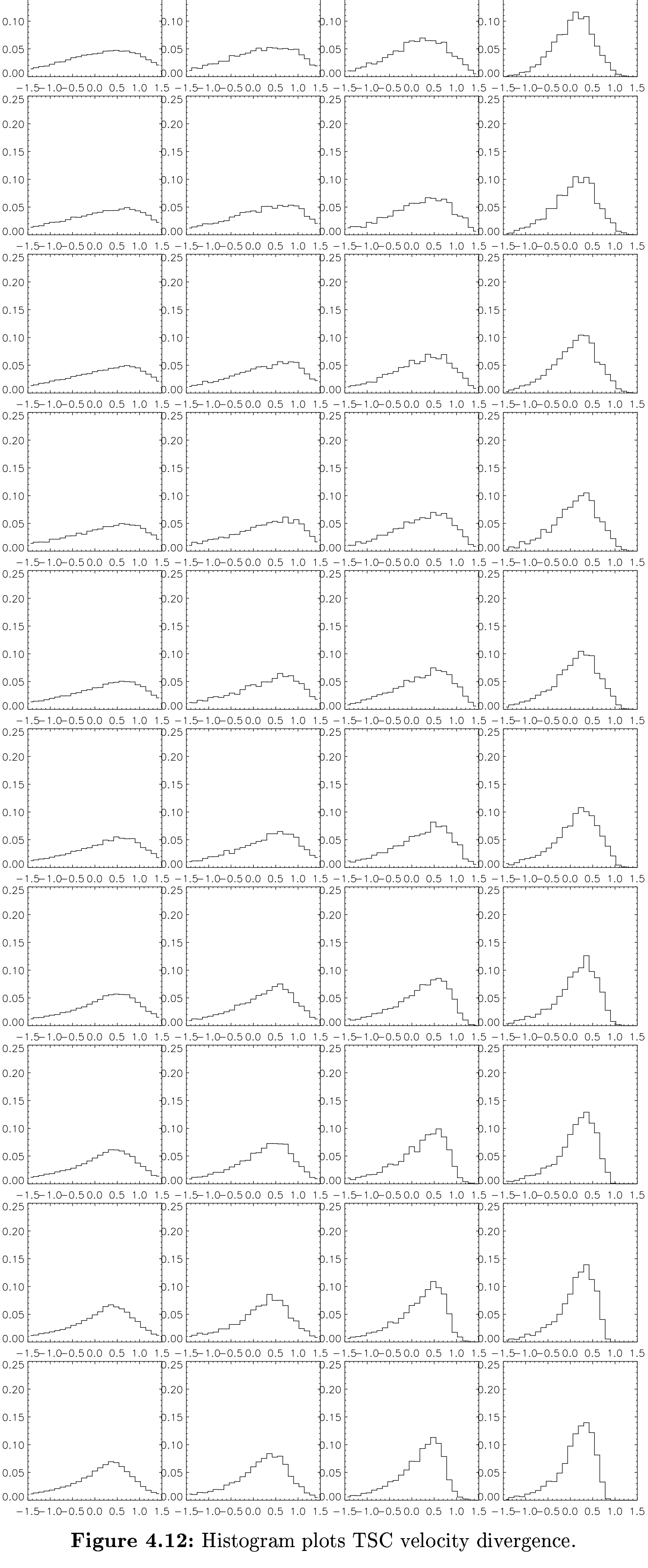

Figure 4.12: Histogram plots TSC velocity divergence.

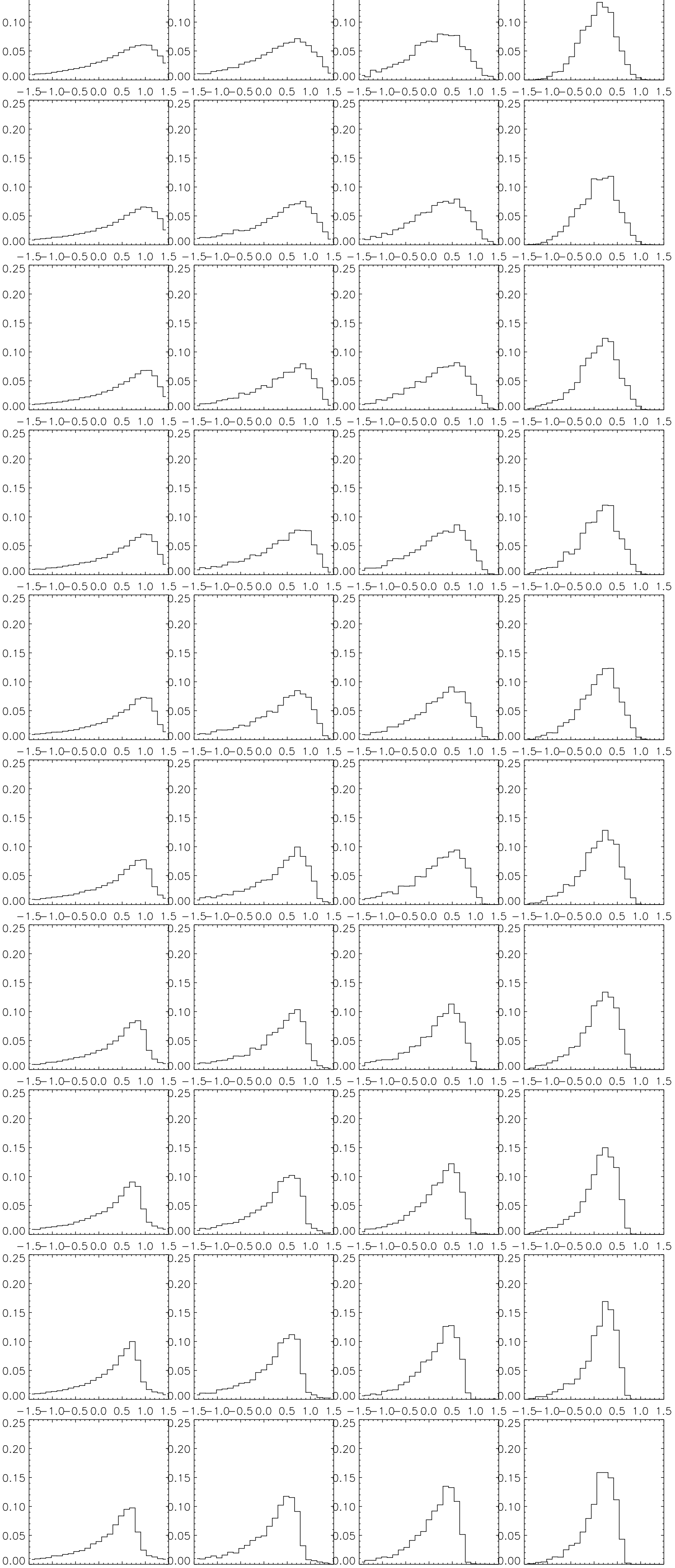

Figure 4.13: Histogram plots DTFE velocity divergence.

Distributions in cumulative plots

Figures 4.15 to 4.16 show the cumulative distributions. On the horizontal axis are the values of the sample points, on the vertical axis its relative number in the sorted array. The value on the vertical axis therefore is the chance P(f) of finding a value lower than f. In these plots, the curves for TSC and DTFE are laid on top of each other with their median values defined to be falling together; at the median value, P(f)=0.5. At large scales, the TSC and DTFE distributions tend to fall together.

Scatterplots and physical relations

To test the relation between the density and the velocity as described in section 2.5, scatterplots were made of $\nabla \cdot \mathbf{v}$ against δ. Figure 4.17 shows these scatterplots of TSC (left) and DTFE (right). For low density-values ($\delta < 0$) I made a linear fit, which is the line in the plots. For the whole range of δ, I made a second-order fit, shown in Figure 4.18. At early times and at very large scales, the relations are expected to be linear-like. At smaller scales, the the points would follow the Bernardeau (second order) relation.

At the last timestep, when $a_{exp} = 1$ (and $z = 0$), we can approximate $f(\Omega)$ with $\Omega^{0.6}$. Now we can put in the linear relation and the quasi-linear approximation of Bernardeau, equations 2.34 and 2.35. Figure 4.14 shows the scatterplots of $\nabla \cdot \mathbf{v}$ against δ, the lines represent both relations. For both methods, the points follow the lines quite nicely in general. Nevertheless, DTFE does not seem to fit in these relations better than TSC. The smoothing scale of 10 Mpc seems to be enough for the Bernardeau relation (which is valid up to $\delta = 2$). Larger smoothing scales would lead to a linear relation.

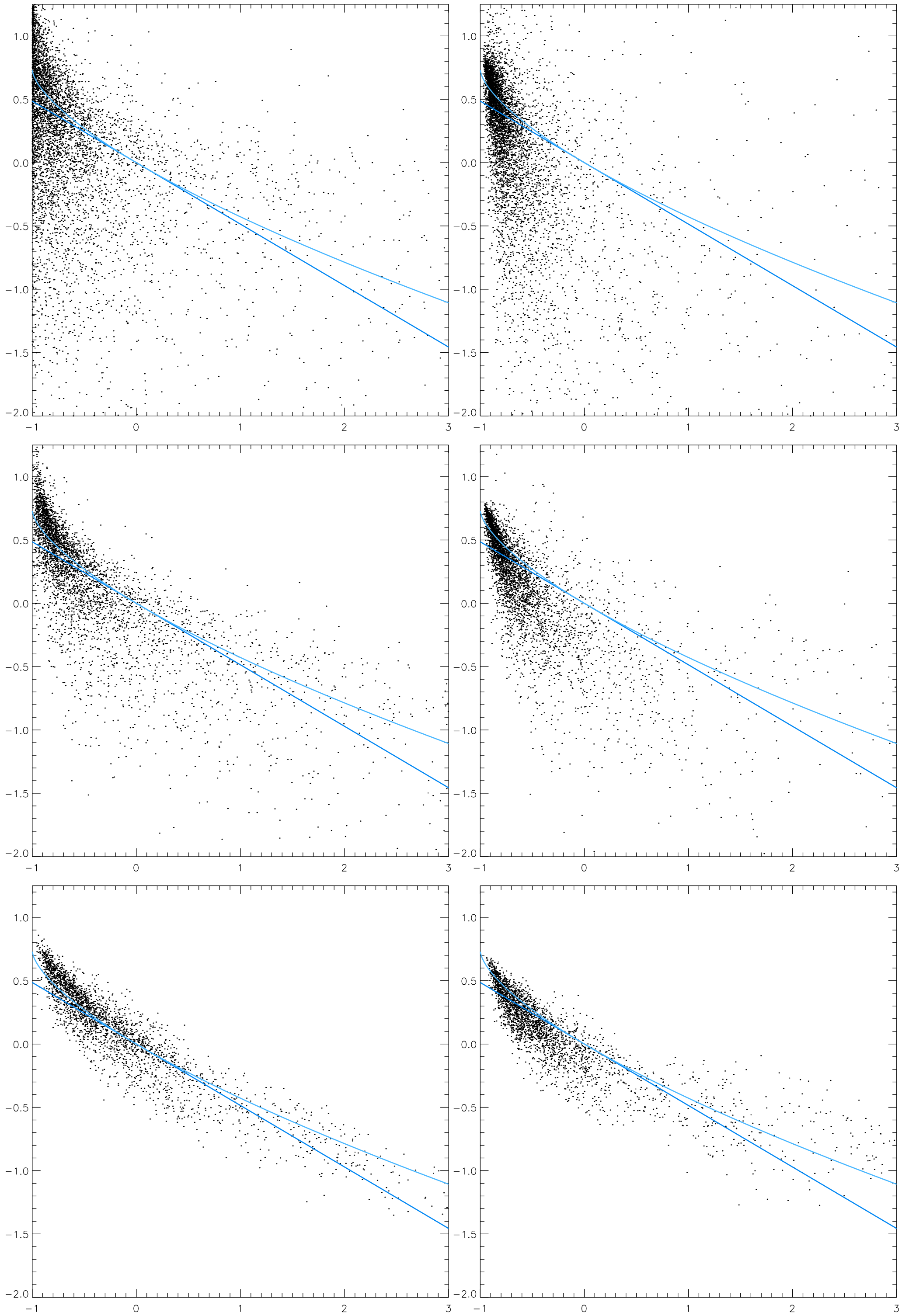

Figure 4.14: Scatter plots of the velocity divergence against δ. From top to bottom smoothing scales 2, 5 and 10 Mpc. Left TSC, right DTFE.

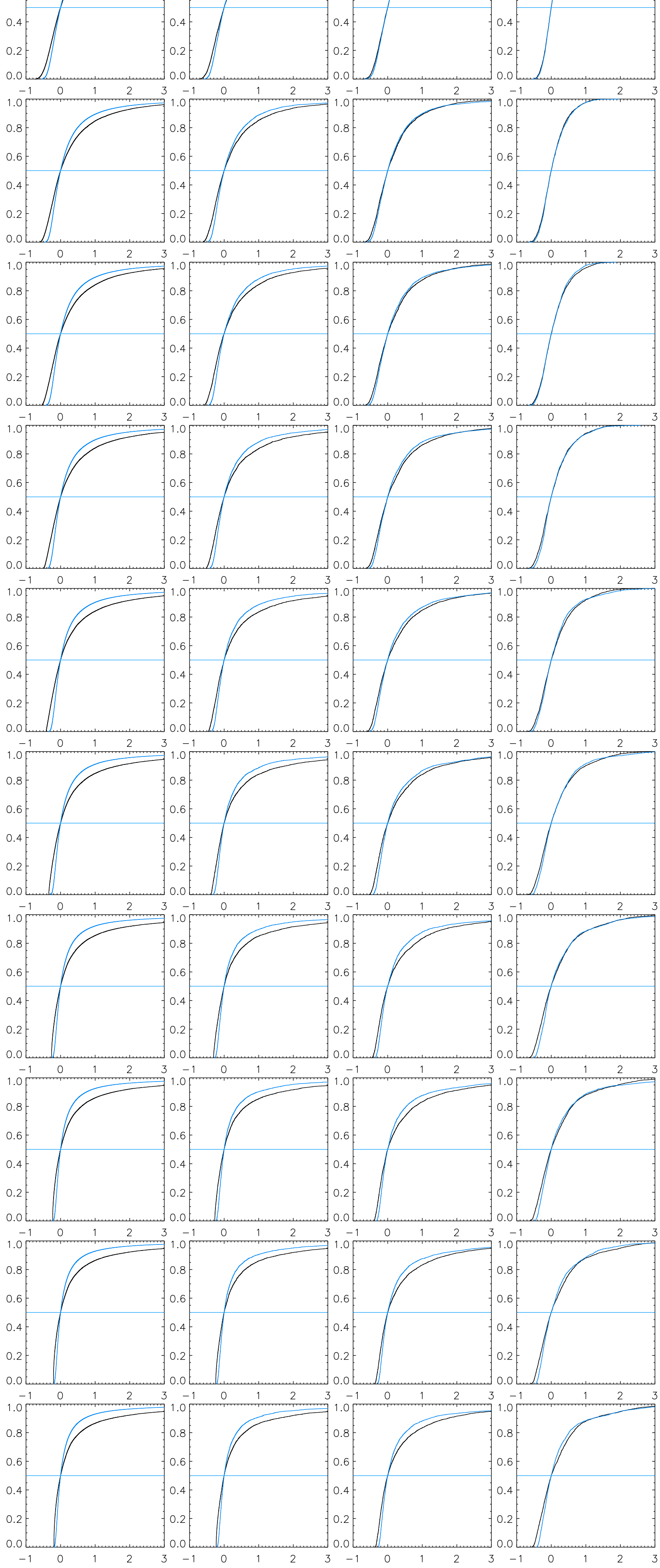

Figure 4.15: Cumulative distributions of density (δ). The black line is for TSC, the blue line is for DTFE. These distributions of TSC and DTFE are laid over each other with their median values falling together, this is what the horizontal lines indicate.

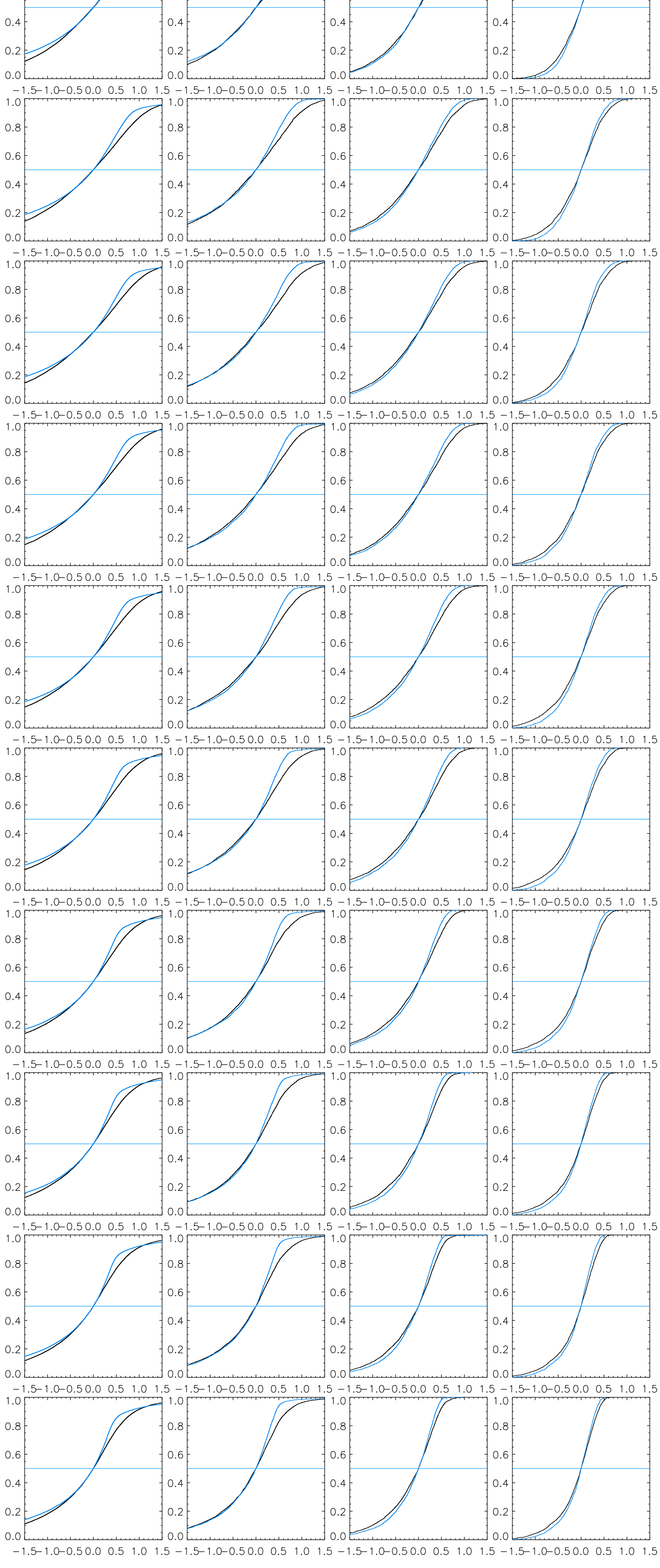

Figure 4.16: Cumulative of the velocity divergence. As in figure 4.15: black denotes TSC, blue denotes DTFE. Medians defined to be falling together, denoted by the horizontal lines.

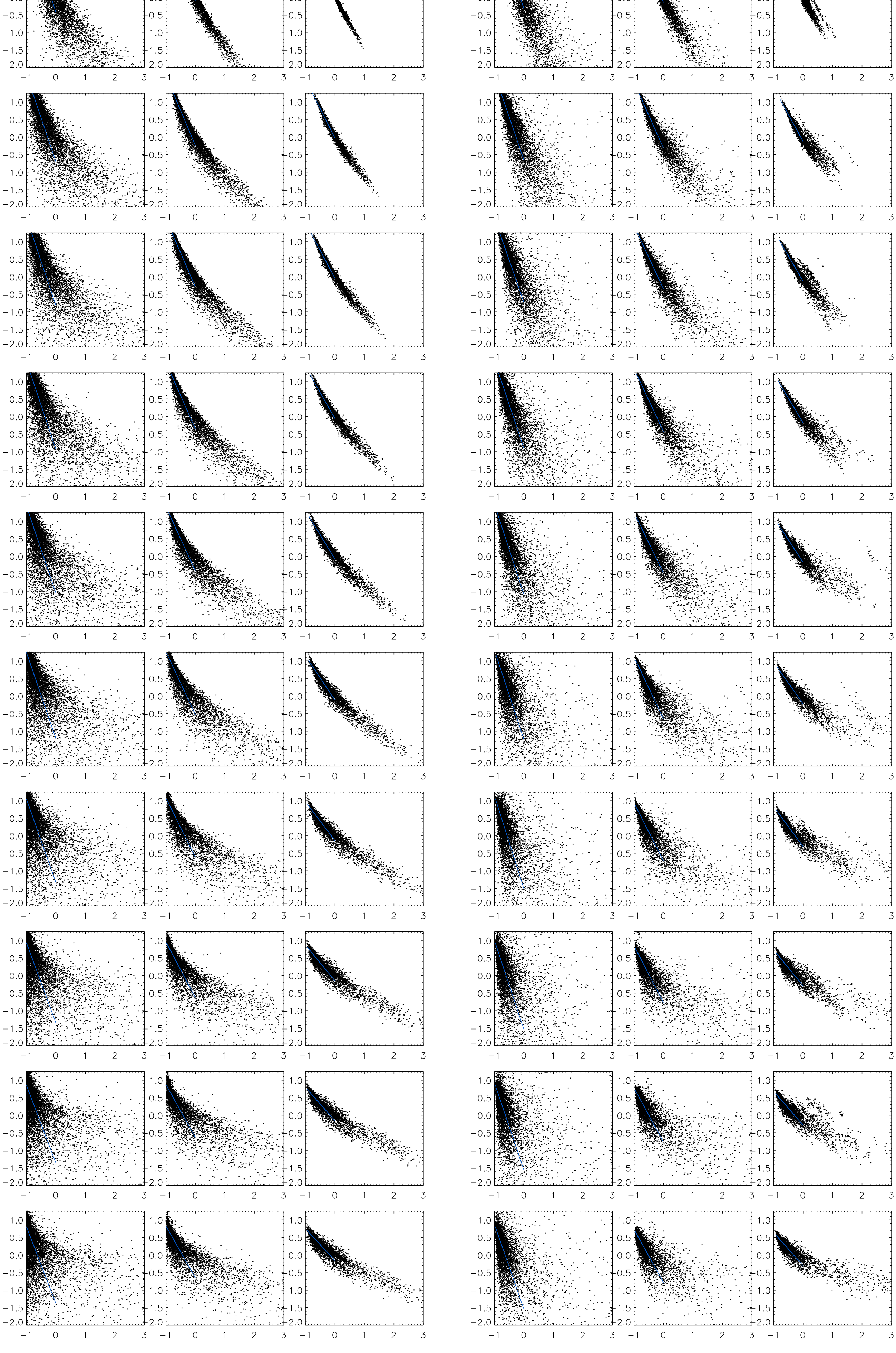

Figure 4.17: Scatterplots of velocity divergence against delta. The blue line is a linear fit for δ between -1 and 0. TSC (left) and DTFE (right).

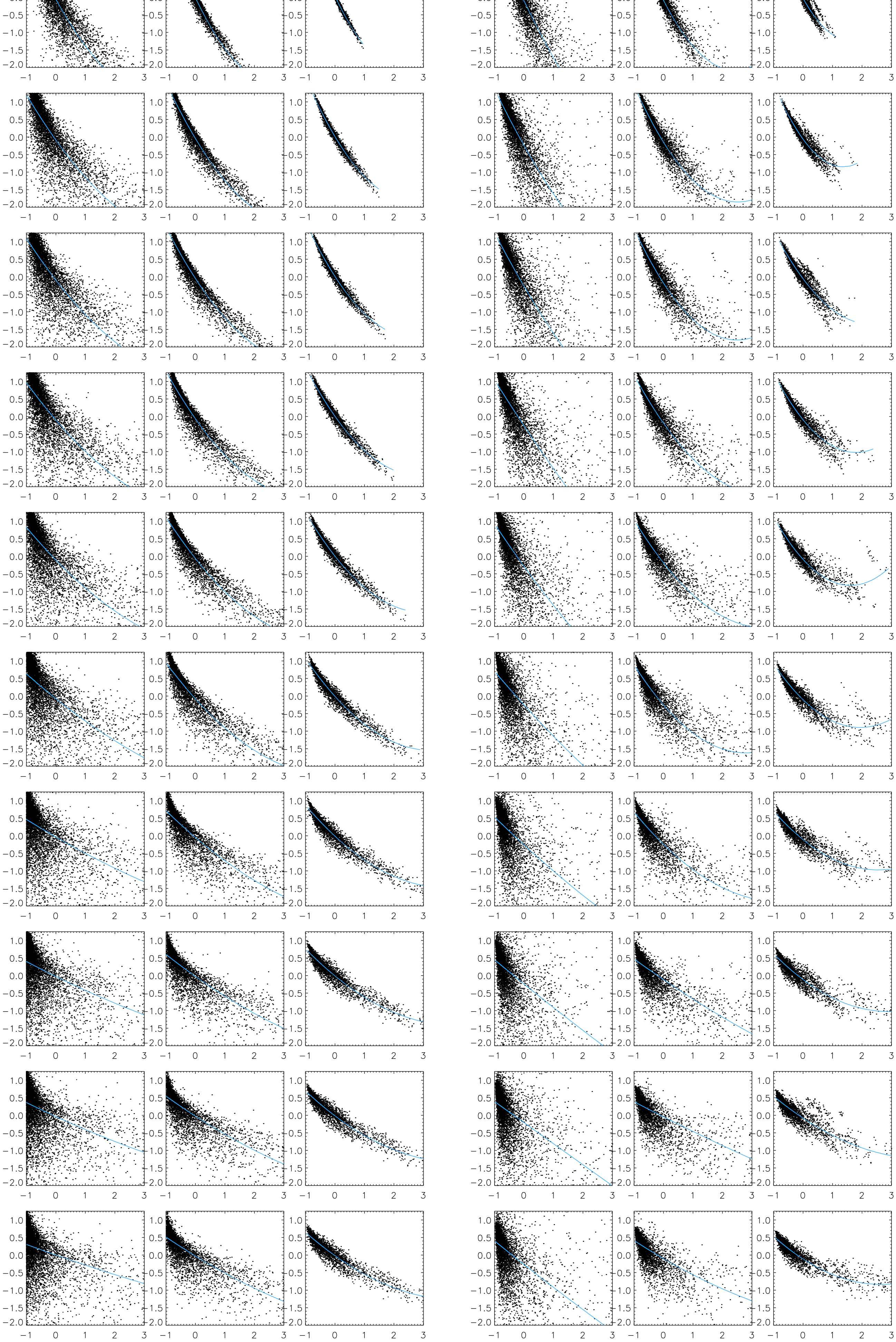

Figure 4.18: Scatterplots of velocity divergence against delta, the line is a second order fit. TSC (left) and DTFE (right).

statistics files
One part of the IDL program calculated statistics of the distributions. For each quantity the mean, median, standard deviation, skewness and kurtosis were written to a file. There are files for each timestep and for each smoothing scale, containing the values for TSC and DTFE. Also the coefficients of the fits of the $\nabla \cdot \mathbf{v}$ relation are written to files. This information can be used for further analysis of the data.

4.4 Summary, discussion and conclusions

The peculiar velocity field on both small and large scales contains valuable information for determining important parameters in cosmology, like Ω. Observations and N-body simulations give discrete distributions. In order to analyse the field and compare with theory, the discrete distribution should be translated to the underlying continuous field. Two examples of methods that recover the volume-averaged field are Triangular Shaped Cloud (TSC) interpolation and the Delaunay Tessallation Field Estimator (DTFE). Previous analyses of these methods indicate that DTFE reconstruction gives a more accurate estimate of the density and velocity fields. Especially in low-dense regions DTFE still provides information, whereas TSC suffers from shot-noise effects.

My task was to derive and display the statistics of the velocity field, comparing those resulting from TSC and DTFE reconstruction of a N-body simulation. For this, I wrote an IDL program that could process the N-body, TSC and DTFE data. This program reads the files containing, for different timesteps, information about particles positions and velocities, the TSC density and velocity field and the DTFE density and velocity field. The velocity gradients for TSC and DTFE were computed. Then the data was smoothed with a top-hat filter for 3 different radii (2, 5, and 10 h^{-1}Mpc). The results were displayed in contour scatter plots, contour plots, vector plots, histogram plots, cumulative plots. Statistics of the quantities were written to files for different time-steps. These figures and statistics can be used for qualitative and quantitative analysis of the density and velocity fields. At first sight, the results do indicate a better performance of DTFE over TSC in the low-dense regions, as expected. But a superior performance is not quite obvious in the relations between density and velocity. However, TSC was used with a 'fair' resolution of 32^3 gridpoints, whereas DTFE can be used with higher resolution. Also, the process of top-hat smoothing was so time-consuming that smoothed values were calculated only for few gridpoints. Further investigation could lead to different results. One could think of using other N-body simulations to compare the results. Smoothing with higher resolution or using other smoothing methods could help. When a box with periodic data is used, smoothing can be performed in Fourier space, which is much faster. Finally, the statistics can be analysed further, in order to properly judge the data (unfortunately, there was no time left for me to this).

Acknowledgements

Hopefully I will not forget anyone, if so: I am sorry, but I am in hurry now! In no preferred order I would like to thank... Rien for introducing me into this most interesting topic. During this research project I certainly have learnt a lot and besides that, I have grown from a non-programmer to a mediocre programmer. Thanks to Willem and Emilio for making the data available for this project, Emilio: no worries, your secret information is still save. The inhabitants and ex-inhabitants of ZG193: thanks for the many discussions about which tea to make or not to make, about the draught in the room and the precise position of the window. I hope you will treat the plants with respect. Edo, thanks for picking me up every morning during the past year. All the people at the institute that made my days more comfortable. Rense for always being a friend. Teffie for non-weakly weekly support in the Roezemoes and Rigoletto in the past, and daily support in the recent past. Friends for all the fun that is necessary. I especially want to thank my family for waiting so long, for support of any kind and for all good thoughts! And Ronald, your never-ending support is a great help, as well as your never-ending funny behaviour. Thanks for meeting me last year!

Bibliography

[1] J. M. Bardeen, J. R. Bond, N. Kaiser, and A. S. Szalay. The statistics of peaks of Gaussian random fields. *ApJ*, 304:15–61, May 1986.

[2] C. L. Bennett, M. Halpern, G. Hinshaw, N. Jarosik, A. Kogut, M. Limon, S. S. Meyer, L. Page, D. N. Spergel, G. S. Tucker, E. Wollack, E. L. Wright, C. Barnes, M. R. Greason, R. S. Hill, E. Komatsu, M. R. Nolta, N. Odegard, H. V. Peiris, L. Verde, and J. L. Weiland. First-Year Wilkinson Microwave Anisotropy Probe (WMAP) Observations: Preliminary Maps and Basic Results. *ApJSupp*, 148:1–27, September 2003.

[3] F. Bernardeau. The quasi-Gaussian density-velocity relationship. *ApJL*, 390:L61–L64, May 1992.

[4] F. Bernardeau and J. Uzan. Non-Gaussianity in multifield inflation. *PRD*, 66(10), November 2002.

[5] F. Bernardeau and R. van de Weygaert. A new method for accurate estimation of velocity field statistics. *MNRAS*, 279:693+, March 1996.

[6] F. Bernardeau, R. van de Weygaert, E. Hivon, and F. R. Bouchet. The Omega dependence of the velocity divergence distribution. *MNRAS*, 290:566–576, September 1997.

[7] E. Bertschinger and A. Dekel. Recovering the full velocity and density fields from large-scale redshift-distance samples. *ApJL*, 336:L5–L8, January 1989.

[8] E. Branchini, L. Teodoro, C. S. Frenk, I. Schmoldt, G. Efstathiou, S. D. M. White, W. Saunders, W. Sutherland, M. Rowan-Robinson, O. Keeble, H. Tadros, S. Maddox, and S. Oliver. A non-parametric model for the cosmic velocity field. *MNRAS*, 308:1–28, September 1999.

[9] S. M. Carroll, W. H. Press, and E. L. Turner. The cosmological constant. *ARAA*, 30:499–542, 1992.

[10] M. Colless. First results from the 2dF Galaxy Redshift Survey. *Royal Society of London Philosophical Transactions Series A*, 357:105+, January 1999.

[11] V. De Lapparent, M. J. Geller, and J. P. Huchra. A slice of the universe. *ApJL*, 302:L1–L5, March 1986.

[12] A. Dekel. Dynamics of Cosmic Flows. *ARAA*, 32:371–418, 1994.

[13] R. H. Dicke, P. J. E. Peebles, P. G. Roll, and D. T. Wilkinson. Cosmic Black-Body radiation. *ApJ*, 142:414–419, July 1965.

[14] A. Einstein. *Zeitschrift für Physik*, 1923.

[15] R. W. Hockney and J. W. Eastwood. *Computer simulation using particles.* Bristol: Hilger, 1988.

[16] Y. Hoffman and E. Ribak. Constrained realizations of Gaussian fields - A simple algorithm. *ApJL*, 380:L5–L8, October 1991.

[17] E. Hubble. A relation between distance and radial velocity among extra-Galactic Nebulae. *Proceedings of the National Academy of Science*, 15:168–173, March 1929.

[18] O. Lahav, M. J. Rees, P. B. Lilje, and J. R. Primack. Dynamical effects of the cosmological constant. *MNRAS*, 251:128–136, July 1991.

[19] S. J. Maddox, G. Efstathiou, and W. J. Sutherland. The APM Galaxy Survey - Part Two - Photometric Corrections. *MNRAS*, 246:433+, October 1990.

[20] S. J. Maddox, G. Efstathiou, and W. J. Sutherland. The APM Galaxy Survey - III. an analysis of systematic errors in the angular correlation function and cosmological implications. *MNRAS*, 283:1227–1263, December 1996.

[21] J. A. Peacock. *Cosmological Physics.* Cambridge University Press, 1999.

[22] J. A. Peacock and A. F. Heavens. The statistics of maxima in primordial density perturbations. *MNRAS*, 217:805–820, December 1985.

[23] P. J. E. Peebles. *The large-scale structure of the universe.* Princeton University Press, 1980.

[24] A. A. Penzias and R. W. Wilson. A measurement of excess antenna temperature at 4080 Mc/s. *ApJ*, 142:419–421, July 1965.

[25] E. Romano-Díaz. Probing Cosmic Flows in the Local Universe. *Ph.D. Thesis*, 2004.

[26] R. K. Sachs and A. M. Wolfe. Perturbations of a Cosmological Model and Angular Variations of the Microwave Background. *ApJ*, 147:73–90, January 1967.

[27] V. Sahni and P. Coles. Approximation methods for non-linear gravitational clustering. *Physrep*, 262:1–135, November 1995.

[28] W. E. Schaap and R. van de Weygaert. Continuous fields and discrete samples: reconstruction through Delaunay tessellations. *A&A*, 363:L29–L32, November 2000.

[29] W. E. Schaap and R. van de Weygaert. Delaunay recovery of cosmic density and velocity probes. In *Statistical Challenges in Astronomy*, pages 483+, 2003.

[30] S. F. Shandarin and Y. B. Zeldovich. The large-scale structure of the universe: Turbulence, intermittency, structures in a self-gravitating medium. *Reviews of Modern Physics*, 61:185–220, April 1989.

[31] S. A. Shectman, S. D. Landy, A. Oemler, D. L. Tucker, H. Lin, R. P. Kirshner, and P. L. Schechter. The Las Campanas Redshift Survey. *ApJ*, 470:172+, October 1996.

[32] M. A. Strauss and J. A. Willick. The density and peculiar velocity fields of nearby galaxies. *Physrep*, 261:271–431, 1995.

[33] R. van de Weygaert. Froth across the Universe. In *ASSL Vol. 276: Modern Theoretical and Observational Cosmology*, pages 119+, September 2002.

[34] R. van de Weygaert and F. Bernardeau. Velocity Fields and Tessellation Techniques: Unbiased Estimators of Omega. In *Large Scale Structure: Tracks and Traces*, pages 207–216, 1998.

[35] R. van de Weygaert and E. Bertschinger. Peak and gravity constraints in Gaussian primordial density fields: an application of the Hoffman-Ribak method. *MNRAS*, 281:84+, July 1996.

[36] R. van de Weygaert and V. Icke. Fragmenting the universe. II - Voronoi vertices as Abell clusters. *A&A*, 213:1–2, April 1989.

[37] Y. B. Zel'Dovich. Gravitational instability: an approximate theory for large density perturbations. *AAP*, 5:84–89, March 1970.

`http://map.gsfc.nasa.gov/m_uni/uni_101fate.html` (expansion figure)
`http://www.nottingham.ac.uk/~ppzsjm/apm/apm.html` (APM website)
`http://pegasus.phast.umass.edu/frame.html` (2MASS image/website)
`http://qold.astro.utoronto.ca/~lin/lcrs.html` (Las Campanas website)
`http://cfa-www.harvard.edu/~huchra/zcat/` (CfA image/website)
`http://www.mso.anu.edu.au/2dFGRS/` (2dF & APM images/2dF website)
`http://www.sdss.org/` (SDSS image/website)
`http://lambda.gsfc.nasa.gov/` (COBE & WMAP image/website)

Appendix A: The velocity gradient in a Delaunay cell

Take a three-dimensional Delaunay cell, defined by the vertex points $\mathbf{r}_0, \mathbf{r}_1, \mathbf{r}_2, \mathbf{r}_3$. The velocity field as seen from Delaunay vertex $\mathbf{r}_0(x_0, y_0, z_0)$, for $n = 1, 2, 3$ is

$$\begin{aligned}
\Delta v_{xn} &= \frac{\partial v_x}{\partial x}\Delta x_n + \frac{\partial v_x}{\partial y}\Delta y_n + \frac{\partial v_x}{\partial z}\Delta z_n \\
\Delta v_{yn} &= \frac{\partial v_y}{\partial x}\Delta x_n + \frac{\partial v_y}{\partial y}\Delta y_n + \frac{\partial v_y}{\partial z}\Delta z_n \\
\Delta v_{zn} &= \frac{\partial v_z}{\partial x}\Delta x_n + \frac{\partial v_z}{\partial y}\Delta y_n + \frac{\partial v_z}{\partial z}\Delta z_n
\end{aligned}$$

with

$$\begin{aligned}
\Delta v_{xn} &\equiv v_{xn} - v_{x0} \qquad & \Delta x_n &\equiv x_n - x_0 \\
\Delta v_{yn} &\equiv v_{yn} - v_{y0} \qquad & \Delta y_n &\equiv y_n - y_0 \\
\Delta v_{zn} &\equiv v_{zn} - v_{z0} \qquad & \Delta z_n &\equiv z_n - z_0
\end{aligned}$$

The nine components of the velocity gradient tensor $\frac{\partial v_i}{\partial x_j}$ now are calculated by

$$\begin{pmatrix} \frac{\partial v_x}{\partial x} & \frac{\partial v_y}{\partial x} & \frac{\partial v_z}{\partial x} \\ \frac{\partial v_x}{\partial y} & \frac{\partial v_y}{\partial y} & \frac{\partial v_z}{\partial y} \\ \frac{\partial v_x}{\partial z} & \frac{\partial v_y}{\partial z} & \frac{\partial v_z}{\partial z} \end{pmatrix} = A^{-1} \begin{pmatrix} \Delta v_{x1} & \Delta v_{y1} & \Delta v_{z1} \\ \Delta v_{x2} & \Delta v_{y2} & \Delta v_{z2} \\ \Delta v_{x3} & \Delta v_{y3} & \Delta v_{z3} \end{pmatrix}$$

where A^{-1} is the inverse of the matrix

$$A = \begin{pmatrix} \Delta x_1 & \Delta y_1 & \Delta z_1 \\ \Delta x_2 & \Delta y_2 & \Delta z_2 \\ \Delta x_3 & \Delta y_3 & \Delta z_3 \end{pmatrix}$$

See also Bernardeau & Van de Weygaert 1996 [5].

Appendix B: Previously done work

For this research project, I first spent an amount of time studying other parts of this subject. In chronological order: I displayed simple statistics of Voronoi Tesselations with Super Mongo. I ran N-body simulations and wrote a program in IDL to graphically display the resulting density and velocity fields in different parts of the simulation cube. Eventually, I also used TSC interpolation for displaying these fields. After this, I applied Voronoi/Delaunay tesselations on the N-body data. I wrote a Fortran code that would combine two files, the file containing the N-body particle data (positions and velocities) and the file containing the data of the Delaunay tesselation (which cells contain which points). This program calculated the velocity gradients within the Delaunay tetrahedra. Combining this with specified locations for which to calculate the velocity would result in the 'continuous' velocity field. However, this code already already had been finished in the mean time. Therefore I turned to the last part, that of deriving the statistics of the velocity field reconstructed with the TSC and DTFE methods.